Applied Physics A (2026) 132:546
https://doi.org/10.1007/s00339-026-09715-8

Applied Physics A
Materials Science & Processing

Harnessing *Alcea biennis* for sustainable and high-performance organic/Inorganic heterojunction photodetectors

Fatma Yıldırım[1] · Ömer Çeçen[2] · Hafize Yuca[3] · Songül Karakaya[4] · Ümit İncekara[5,6] · Şakir Aydoğan[1]

Received: 22 January 2026 / Accepted: 5 May 2026 / Published online: 26 May 2026

Abstract

Herein, we demonstrate self-assembled, highly stable, high-performance, and broadband response organic/inorganic hybrid photodetectors based on AB@Si devices formed by the integration of both n-type and p-type Si with *Alcea biennis* (AB) extract. Besides, recombination currents and traps were observed to be more effective in the AB@p-Si device. Both devices were found to exhibit remarkable photoresponse under illumination conditions in the white light as well as in UV and IR. The AB@n-Si device exhibited impressive performance metrics at -2.0 V, with the responsivity (R), detectivity (D), and external quantum efficiency (EQE) reaching 758 mA/W (at 365 nm), 2.42×10^{11} Jones (at 590 nm), and 250% (at 365 nm), respectively. Under the same bias conditions, the AB@p-Si device exhibited enhanced performance, yielding a responsivity of 1384 mA/W, a detectivity of 4.66×10^{11} Jones, and an EQE of 282%, all recorded at 590 nm. It was seen that the integration of AB with n-Si and p-Si holds promise for high-performance, very stable, low-cost organic/inorganic-based devices with different designs.

Keywords *Alcea biennis* · Plant extract · Detectivity · Organic-inorganic hybrid photodetector · Broadband

1 Introduction

Photodetectors (PDs) are types of light sensors frequently used in applications such as image processing and energy conservation. They are key components of various optoelectronic devices that convert incident photons of different energies into modulatable electrical signals [1]. In general, PDs can be classified as broadband (panchromatic) or narrowband (wavelength selective) depending on the wavelength at which they absorb light. Broadband PDs are expected to cover a wide wavelength range from the ultraviolet-visible (UV-Vis) region to the near-infrared (NIR) region, while narrowband PDs are expected to cover a specific light range such as red, green, blue, or a selective portion of NIR [2].

Inorganic semiconductors such as Si, InGaAs and GaAs have undoubtedly been used in electronic or optoelectronic-based devices for years due to their small exciton binding energy, excellent charge-carrier mobility, and high stability [3]. Besides, tuning the parameters of conventional silicon-based semiconductor devices is mainly achieved by doping the semiconductor through complex and costly processes or by adding microstructures such as superlattices [4]. Complex manufacturing processes, their hardness and brittleness, the fact that they are produced at high temperatures, the presence of toxic elements such as Cd and Pb in some cases, and difficulties in integrating them into heterojunction structures are among the negative aspects that may limit the use of inorganic materials in electronics. The lack of flexibility and high cost of inorganic semiconductors such as silicon and GaAs, which are commonly used in photodiodes or photodetector applications, are significant disadvantages.

✉ Şakir Aydoğan
saydogan@atauni.edu.tr

[1] Department of Physics, Science Faculty, Atatürk University, 25240 Erzurum, Türkiye

[2] Department of Plant and Animal Production, Vocational School of Technical Sciences, Karamanoğlu Mehmetbey University, Karaman, Türkiye

[3] Department of Pharmacognosy, Faculty of Pharmacy, Ataturk University, Erzurum, Türkiye

[4] Department of Pharmaceutical Botany, Faculty of Pharmacy, Ataturk University, Erzurum, Türkiye

[5] Department of Mol Biol & Genet, Science Faculty, Erzurum Technical University, Erzurum, Türkiye

[6] Department of Biology, Science Faculty, Ataturk University, Erzurum, Türkiye

As an alternative to these disadvantages, research has been conducted for years on low-cost, flexible, large-area, and lightweight organic materials [5]. Organic semiconductor materials have been widely used in energy conversion and electronics applications for over two decades, and their use has led to significant advances in both materials design and device engineering [6]. They have lower charge mobility and a lower dielectric constant than inorganic materials. This lower dielectric constant can lead to the formation of highly localized, tightly bound Frenkel excitons (electron-hole pairs) upon photoexcitation [7].

Photovoltaic devices based on organic semiconductors such as solar cells, indoor photovoltaic cells, photodiodes, and photodetectors hold great promise due to their many advantageous aspects, such as sustainable energy, good optical properties and light harvesting technologies [8–12]. Other features that make these materials stand out are their ease of use in device manufacturing, versatility of functionalization, a low-temperature fabricating process, flexibility and ability to enable large-scale production [4, 13–15]. Many organic-based photodetectors also offer the possibility of operating at room temperature [7]. Because of these advantages, solution-processed semiconductors, such as organic semiconductors, are increasingly being used as alternatives to traditional inorganic semiconductors, or they are increasing their potential use. However, organic materials also have disadvantages such as low mobility, low responsivity, recombination and trapping due to irregular crystal structures in some cases, as well as stability issues, which may limit their use in optoelectronics. Despite the disadvantages of organic and inorganic materials, their respective advantages have been combined according to their intended use, making them widely used, especially for broadband photodetector applications [16–18]. Organic materials also have the advantage of being easily integrated with various inorganic materials. The development of organic-inorganic hybrid materials has made significant contributions to science in terms of materials and device science. In recent years, organic-inorganic hybrid semiconductors have shown great promise in the field of optoelectronics due to their wide absorption spectrum, high photovoltaic conversion efficiency, structural flexibility, and multifunctionality. Hybrid structures have emerged as a promising strategy to overcome the intrinsic limitations of pure inorganic or organic photodetectors, offering enhanced responsivity and a broader spectral range from UV to NIR [19]. Hybrid systems combine the high carrier mobility of inorganic semiconductors with the processability/flexibility of organic components. The *AB*/Si device fits this mechanism: polyphenols/anthocyanins/flavonoids (e.g., kaempferol glycosides such as tiliroside known from *Alcea* spp.) can extend absorption and lower the interfacial barrier, while n-Si (or a comparable inorganic) supplies low-noise transport and stability, together yielding large NPDR and fast, self-powered properties [20]. (Chemical structure of *trans*-tilirosid and general chemical structure of anthocyanins have been given in Fig. 1a and b.). The use of hybrid materials is not limited to photodetectors; they have the potential to be used in many different fields [21]. More importantly, in hybrid-based photodetectors, not only the fundamental properties of each material but also the structure of the interface between the two materials is crucial for device performance. This interface may exhibit changes due to interactions between the dangling bonds or thin oxide layer on the surface of the inorganic material and the organic material, as well as different structural changes depending on the properties of the chemical bonds resulting from chemical interactions between the two materials.

Recently, plant extract-based organic optical devices have attracted significant interest due to their high performance, ease and low cost of synthesis, abundance, and environmentally friendly properties [22–26]. Literature on natural-dye optoelectronics supports this interpretation. Plant-derived pigments (anthocyanins, betacyanins, flavonols) possess anchoring –OH/–COOH groups and conjugated chromophores that promote charge transfer at oxide/Si surfaces—principles established in Dye-sensitized solar cells (DSSCs) and bio-optoelectronic reviews and demonstrated specifically for *A. rosea* and related botanicals. Efficient extraction and use of *Alcea* pigments for light-harvesting have been reported, and broad surveys document how dye chemistry, pH, and extraction route tune spectral coverage and interfacial energetics—factors that likely underpin your broadband response and high on/off ratio [27]. *A. biennis* Winterl a perennial or occasionally short-lived herbaceous species belonging to the family Malvaceae. The plant exhibits erect, generally unbranched stems covered with stellate (star-shaped) and tufted hairs, giving the surface a distinctly rough texture [28].

Although there are different methods for integrating organic materials into inorganic materials, the spin coating method stands out due to its low cost and ease of film coating [29]. This method does not require vacuum and facilitates the mobility of carriers by producing a homogeneous film. Additionally, the film thickness, rotation speed, rotation time, and solution viscosity can be easily adjusted.

With this aim, it is also possible to produce a photodetector operating in a broadband using a heterojunction structure created with a different inorganic semiconductor. With this in mind, the main objective of this study is to conduct a detailed analysis of the broadband photodetector performance of heterojunctions formed with *Alcea biennis* (AB) extract, which has a 2.73 eV bandgap, and both n-type and p-type Si, which has a 1.12 eV bandgap.

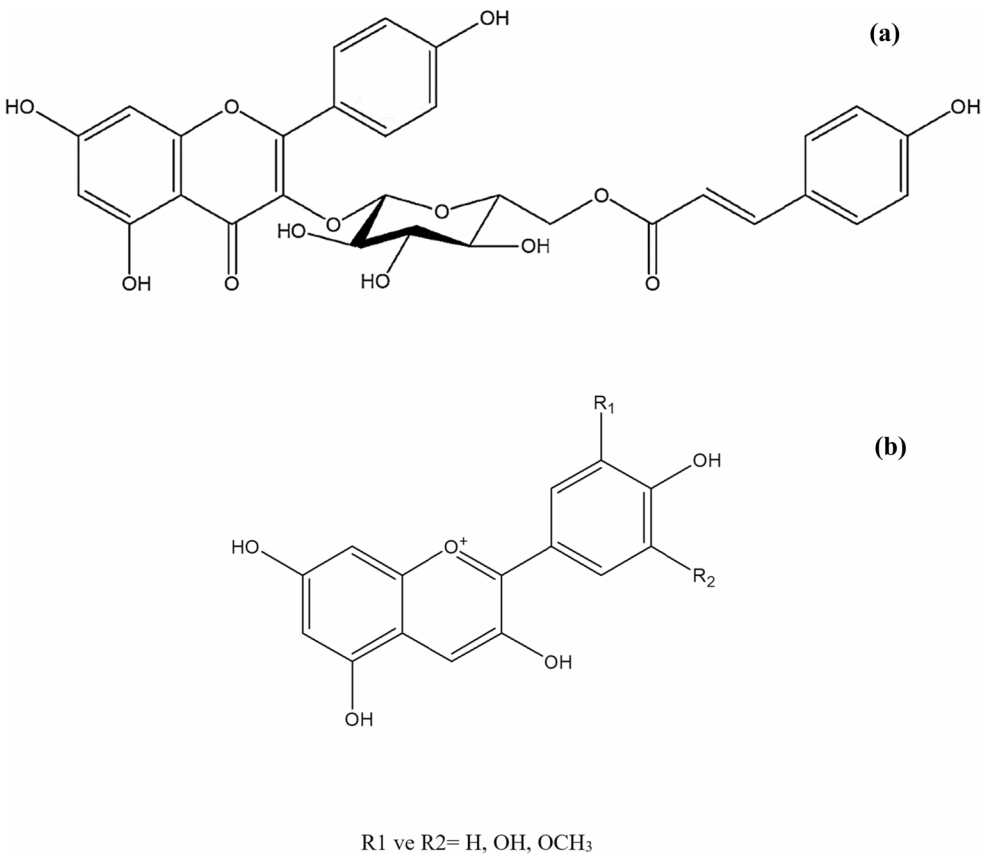

Fig. 1 (**a**) Chemical structure of *trans*-tilirosid and (**b**) General chemical structure of anthocyanins

Recent advances in bio-inspired optoelectronic materials have highlighted the potential of plant-derived chromophores as functional components in photodetector applications, owing to their rich π-conjugated systems and environmentally sustainable nature. Natural pigments such as anthocyanins and flavonoids have been widely investigated for their light-harvesting capabilities and ability to facilitate interfacial charge transfer in hybrid systems [30–34].

In this context, several studies have explored the optoelectronic potential of plant extracts in organic–inorganic hybrid photodetectors. For instance, plant-based systems such as *Hibiscus sabdariffa* have been shown to enhance interfacial charge transport and broadband photoresponse characteristics in hybrid devices [20]. However, despite these advances, studies focusing specifically on *A. biennis* remain very limited, and systematic investigations of wavelength-dependent photoresponse behavior (spectral sensitivity) for this species are still lacking.

Although elemental analysis provides information on inorganic composition, it does not directly identify the molecular species responsible for the observed photoactivity. In *Alcea* species, extensive phytochemical investigations have consistently demonstrated the predominance of phenolic compounds, including flavonoids, anthocyanins, phenolic acids, and mucilage-associated bioactive components [35–37]. These compounds, particularly flavonoids and anthocyanins, possess extended π-conjugated systems that are highly relevant for light absorption and charge transfer processes in optoelectronic applications.

Multiple studies have confirmed the rich and diverse chemical composition of *Alcea* species across different plant organs and extraction methods. For instance, solvent-dependent extraction studies have shown that *Alcea* extracts contain significant amounts of bioactive phenolics and exhibit strong biological activities [38–40]. Organ-specific analyses further indicate that flowers are particularly enriched in polyphenolic compounds, while seeds and other tissues may contain fatty acids and additional bioactive constituents contributing to overall chemical complexity [41, 42]. Additionally, advanced extraction approaches such as supercritical CO_2 have revealed the presence of diverse chemical constituents with functional activity, further supporting the compositional richness of the genus [43]. Furthermore, environmental and stress-related studies have demonstrated that *Alcea* species actively modulate their chemical composition under external stimuli, producing various secondary metabolites with functional roles [44]. Encapsulation and formulation studies also confirm the stability and functional importance of polyphenol-rich extracts, emphasizing their structural and chemical integrity. Encapsulated powders of Alcea flower polyphenol-rich extract by different

hydrocolloid carriers. Similarly, pharmacological and biochemical investigations highlight the biological relevance of these compounds, including antioxidant, anti-inflammatory, and protective effects [45].

The UV–Vis absorption behavior observed in the AB thin film is consistent with π–π* transitions typically associated with conjugated phenolic systems. In addition, functional groups such as hydroxyl and carbonyl moieties, commonly reported in *Alcea* extracts, further support the presence of flavonoid-type compounds contributing to interfacial charge transfer processes. Recent studies have also explored the conversion of *Alcea*-derived materials into functional nanostructures, such as carbon dots, demonstrating their applicability in photothermal and optoelectronic contexts [46]. However, it should be emphasized that direct identification and quantification of individual chromophoric compounds (e.g., via HPLC or LC–MS/MS) were not performed in this study. Therefore, the interpretation of structure–property relationships is based on well-established phytochemical classes characteristic of the *Alcea* genus, rather than specific molecular entities. The observed device performance is thus attributed to the collective electronic and interfacial effects of multiple conjugated compounds naturally present in *Alcea biennis*.

Therefore, the novelty of the present study lies not in the general use of plant-derived materials, but in the comprehensive evaluation of wavelength-dependent photoresponse (UV–Vis–IR) of *A. biennis*, including detailed analysis of responsivity, detectivity, and external quantum efficiency, as well as the comparison of interfacial charge transport in n-type and p-type Si heterojunctions.

2 Experimental

AB specimens were collected on 21 June 2019 from the area between Keşişlik and Karalar Koyu, Ermenek (Karaman, Türkiye) at an altitude of approximately 1100 m. The plant material was identified and deposited in the Herbarium of Karamanoğlu Mehmet Bey University under the voucher code KMUB 5335.

2.1 Extraction

Ten grams of dried flowers of *AB* were subjected to maceration with 50 mL of distilled water for three consecutive days, with each extraction cycle lasting 8 h. At the end of each cycle, the aqueous extract was filtered and stored at − 80 °C until all portions were combined and lyophilized. Following freeze-drying, the total yield of the aqueous extract was 3.23 g. A stock solution (1 mg/mL) of the lyophilized extract was subsequently prepared for use in the analytical assays [47].

2.2 Elemental analysis

Elemental concentrations were determined using an inductively coupled plasma–mass spectrometer (ICP–MS; Agilent 7800 Series, Agilent Technologies, Japan). Sample introduction was achieved via a U-series glass MicroMist nebulizer (Australia) coupled with a double-pass quartz spray chamber (USA) to ensure efficient aerosol generation and delivery into the plasma. The plasma system comprised a 2.5 mm quartz torch and nickel sampler and skimmer cones, optimized with an x-lens interface for enhanced ion transmission and sensitivity. All components in contact with the samples were rigorously cleaned to prevent contamination. Quartz and glass parts were immersed overnight in 5–10% HNO_3, rinsed thoroughly with distilled water, dried, and reassembled. Nickel parts underwent ultrasonic cleaning in pure water, 5% HNO_3, and distilled water for 5 min each, followed by drying and reinstallation. Before analysis, the instrument was purged with helium gas for 45 min to remove residual gases and stabilize the system. Calibration was performed using certified multi-element tuning solutions, and calibration curves were verified within standard reference ranges to ensure analytical accuracy. Samples were introduced using an autosampler, and all tubing and probes were thoroughly rinsed between runs to prevent cross-contamination. Analytical parameters such as RF power, carrier gas flow, and nebulizer pump speed were optimized prior to measurement. Argon gas was used as the carrier to transport the aerosol into the plasma, where ionization occurred, followed by precise mass spectrometric detection under controlled operating conditions [48].

2.3 Device fabrication

In device fabrication, single-sided polished n-type and p-type Si wafer plates with a thickness of 280 mm and resistivity values of 1–10 Ω.cm were used. Approximately 1 cm × 1 cm pieces were cut from both wafers, and chemical processes standard for Si, as detailed in Ref [49]., were performed. Aluminum ohmic contacts ∼100 nm thickness were vapor-deposited onto the polished surfaces of the wafers, and AB was spin-coated onto both n-Si and p-Si wafers at 3000 rpm for 60 s. The Au top contacts, with a diameter of 1 mm, were deposited onto the polished surface of the Si substrate by thermal evaporation using a shadow mask to form patterned electrodes. The photoelectric measurements of the devices were performed using a Keithley 2400 source meter under both white light and UV and IR light at different wavelengths. All electrical measurements were performed in the atmospheric conditions of the room without any encapsulation or other protection, while the I-V measurements in the dark were performed in a closed box

where the devices would not be exposed to light. The measurements of the devices under white light as a function of varying light intensity, as well as under UV and IR light, were analyzed in detail.

3 Results and discussion

The use of a simple three-day, three-cycle maceration of 10 g dried *AB* flowers in 50 mL of distilled water, followed by filtration, − 80 °C storage and lyophilisation (yielding 3.23 g extract and prepared as a 1 mg/mL stock) aligns well with conventional practices in phytochemical extraction. Maceration is widely regarded as a low-cost, mild technique for extracting heat-sensitive bioactives such as flavonoids and phenolic acids, albeit with the caveat of relatively lower yields and longer extraction times compared with more aggressive methods [50]. The multiple 8-hour soak intervals used here facilitate sufficient solvent-solid contact and diffusion of soluble compounds into the aqueous medium, while freezing and lyophilisation preserve the extract's chemical integrity. According to the literature, key factors such as solvent-to-solid ratio, extraction time and sample drying state are critical determinants of extract composition and yield [51]. Although the yield of ~ 32% (3.23 g from 10 g starting material) is relatively modest, it is acceptable for aqueous maceration of plant material rich in mucilaginous or hydrophilic constituents, and the subsequent stock solution provides a standardized basis for downstream bioassays. In sum, this protocol offers a suitable compromise between extract quality and simplicity, especially when the goal is to capture a broad extract for analytical and biological screening rather than to isolate single compounds.

The elemental composition of the *AB* aqueous extract (Table 1) reveals a predominance of potassium (K), magnesium (Mg), and calcium (Ca) among the macroelements, consistent with the mineral profiles typically observed in Malvaceae species. Potassium was identified as the most abundant element (10,758.20 g/kg), highlighting its physiological importance as an osmoregulatory and enzymatic cofactor in plant metabolism. Magnesium (4,635.15 mg/kg) and calcium (1,606.94 mg/kg) were also present in considerable amounts, reflecting their roles in photosynthetic processes, cell-wall stabilization, and ion balance. Among the trace elements, zinc (Zn) was detected at relatively high levels (1,347.96 mg/kg), followed by lead (Pb) and copper **(Cu)** at 10.20 mg/kg and 2.38 mg/kg, respectively. The measurable zinc content suggests potential contributions to the plant's antioxidant and enzyme-regulating capacity, whereas the low concentrations of lead and copper remain within typical ranges for plants growing under non-polluted environmental conditions.

Table 1 The composition of elemental analysis of *AB* extract

Major elements (g/kg)	Trace elements (mg/kg)	Ultratrace elements (µg/kg)
K 10758.200	**Mg** 4635.149	**Na** < 0.000
Ca 1606.939	**Zn** 1347.962	**Al** < 0.000
	Pb 10.203	**Fe** < 0.000
	Cu 2.383	**As** < 0.000
		Hg < 0.000
		Ag < 0.000

According to the IUPAC Compendium of Chemical Terminology (2nd edition), a trace element is defined as "any element with an average concentration of less than approximately 100 ppm (parts per million) atoms or below 100 µg/g." However, continual advances in modern analytical instrumentation have significantly increased the sensitivity and precision of elemental detection. As a result, the conventional upper limit defining "trace" concentrations has become insufficient to describe the levels now routinely measurable. To address this, the concept of ultra-trace analysis has emerged, generally referring to determinations at concentration levels below 10^{-6} g/g (1 ppm) and often extending down to 10^{-8} g/g (10 ppb). Although no universally accepted numerical boundary exists, this term broadly encompasses analyses conducted at concentration ranges beyond the conventional trace domain, reflecting the enhanced detection capabilities of contemporary analytical techniques [52]

Notably, ultratrace elements—including sodium (Na), aluminum (Al), iron (Fe), arsenic (As), mercury (Hg), and silver (Ag)—were all below the detection limit (< 0.000 µg/kg), demonstrating the high purity of the sample and the absence of toxic metal accumulation. Such findings underscore the environmental safety and potential nutraceutical suitability of *AB* extracts.

The UV-Vis spectrum obtained from the film on glass and the Tauc curve derived from it are shown in Fig. 2a and b, respectively. Absorbance measurements clearly show that the *AB* film exhibits high absorption, particularly in the UV region. The optical band gap obtained from the Tauc plot was calculated to be 2.73 eV. Furthermore, top view and lateral scanning electron microscope (SEM) images of the AB film on the Si substrate are given in Fig. 2c and d, respectively. As can be seen in Fig. 2c that the image reveals a granular surface morphology characterized by the formation of nanometer-sized clusters. The AB film exhibits a dense and continuous network, which is essential for ensuring efficient charge transport across the organic/inorganic interface. Furthermore, the high surface-to-volume ratio provided by this interconnected granular structure is expected to enhance the light-harvesting capability of the heterojunction. No significant micro-cracks or large-scale defects were observed, confirming the high structural integrity of the fabricated thin film. The cross-sectional SEM analysis reveals that the Alcea biennis (AB) organic layer has a uniform thickness of approximately 104 nm (Fig. 2d). This nanometric thickness is well-suited for high-performance photodetectors, as it is thick enough to ensure significant light absorption while

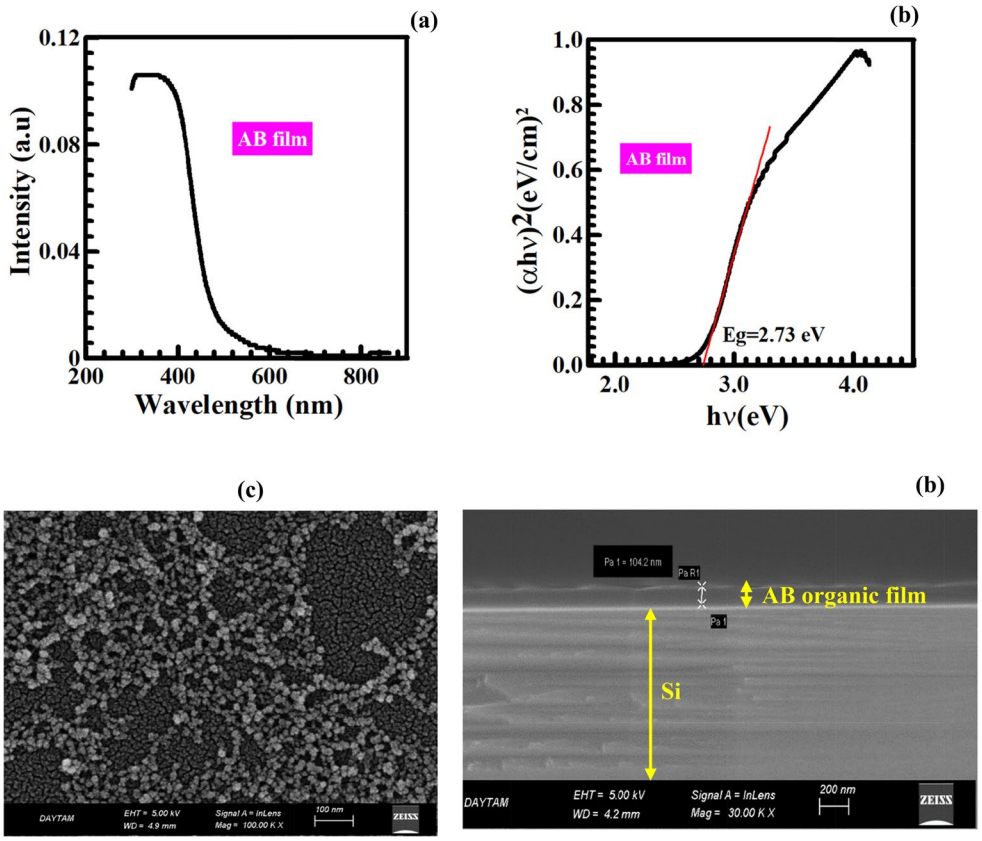

Fig. 2 (**a**) UV/Vis spectra, (**b**) The Tauc plot obtained from the UV–Vis analysis of the *AB* thin film, showing the fitting method for the linear region where the band gap is obtained from the x-axis intersection point, is approximately 2.73 eV here. (**c**) Top-view and (**d**) lateral SEM image of the AB/n-Si heterostructure

remaining thin enough to minimize the series resistance and allow for efficient charge carrier extraction to the electrodes without excessive recombination losses.

The current-voltage graphs of AB@n-Si and AB@p-Si heterojunction devices prepared under the same conditions and measured in the dark and in the ± 2 V range are shown in Fig. 3a. It can be seen that both devices exhibit asymmetric graphs that will provide a fairly high rectification ratio. Although the reverse-bias currents of both devices exhibit similar behavior, the forward-biased current of the AB@n-Si device has a higher slope than AB@p-Si. This indicates that the AB@n-Si device has an advantage over the AB@p-Si device in terms of power consumption since the forward current of the AB@n-Si device at the same bias is higher than that of the AB@p-Si device for the same bias values. The high AB@n-Si current in the forward bias was attributed to the low series resistance and ideality factor, and the high charge carrier injection efficiency with respect to the AB@p-Si heterojunction. Besides, in the range of ± 2, the rectification ratio of AB@n-Si is 4.45×10^5, while that of AB@p-Si device is 8.22×10^4. The ideality factor, which is an important parameter for rectifier devices, is also obtained as 1.57 and 4.0 for AB@n-Si and AB@p-Si devices, respectively, using thermionic emission theory [53]. The value of *n* greater than unity is explained by the difference in the ideal current mechanism for both devices. The value of 1.74 indicates that recombination currents are partially effective in addition to diffusion, while the value of 4.0 is attributed to the non-homogeneous barrier height and the trapping of charge carriers due to the presence of a high-density defects between AB and p-Si in addition to the recombination current [54]. The distinct ideality factors, n = 1.57 for AB@n-Si and n = 4.0 for AB@p-Si, provide critical insight into the interface quality and charge transport dynamics of the devices. The lower ideality factor of 1.57 for AB@n-Si suggests a more ordered interface with fewer recombination centers, which is consistent with its superior rectification ratio. In this device, the current is dominated by thermionic emission with minimal leakage, leading to a more efficient potential barrier. Conversely, the high ideality factor of 4.0 for AB@p-Si indicates a high density of interface states and trap-assisted recombination/tunneling mechanisms [55–57]. This high trap density facilitates a significant photocurrent enhancement through a 'photoconductive gain' mechanism; under illumination, trapped carriers at the AB@p-Si interface can modulate the depletion width or prolong carrier lifetimes, resulting in the impressive responsivity observed. Consequently, while the AB@n-Si device shows a more 'ideal' diode behavior, the AB@p-Si device leverages its trap-dominated interface to achieve enhanced photo-sensing capabilities. To clarify the current conduction mechanisms, the I-V characteristics of both devices were

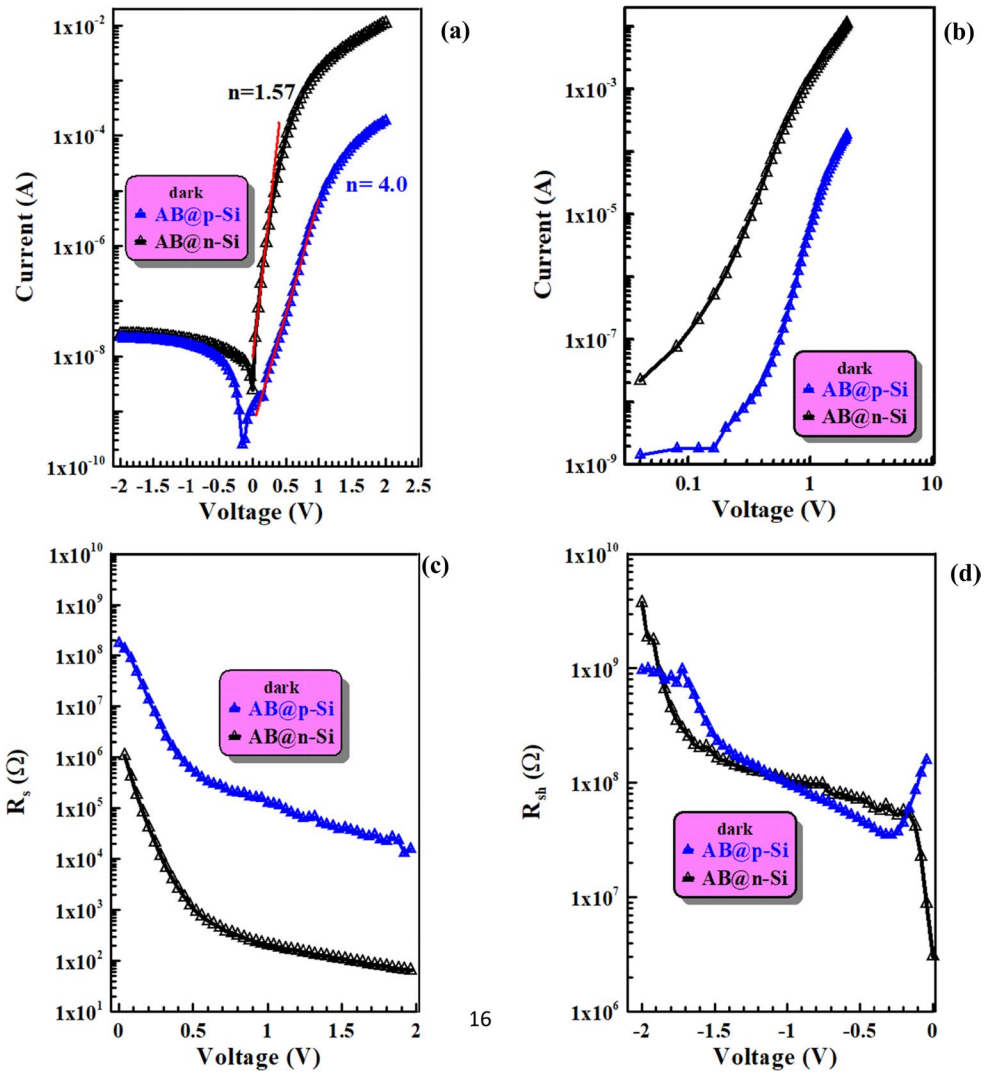

Fig. 3 (**a**) I-V plots of AB@n-Si and AB@p-Si devices in the dark, (**b**) R_s-V plots, (**c**) R_{sh}-V plots in dark, and (**d**)

analyzed on a logarithmic scale (Fig. 3b). For AB@p-Si, the log(I) - log(V) analysis of the forward bias characteristics reveals three distinct conduction regions, which explain the deviation from the ideal TE model. At low voltages(V < 0.2 V), the slope log(*I*) - log(*V*) plot is found to be ≈1.2. This indicates that the current is dominated by thermally generated carriers. At 0.2 V < V < 0.7 V range, the current shows a superlinear dependence ($I \propto V^m$, where m > 2), which is characteristic of a trap-limited SCLC regime [58]. In this region, injected carriers are progressively captured by trap states at the organic/inorganic interface, leading to a deviation from ideal quadratic behavior. The transition from Ohmic to TFL and finally to the SCLC regime provides a comprehensive physical explanation for the non-ideal diode behavior and the impressive photoresponse observed in the AB@p-Si heterostructures. At higher voltages (for V > 0.7 V), the slope settles to 2.2. This confirms that once the traps are filled, the current becomes space-charge limited (SCLC), following the Mott-Gurney law (Child's Law) ($I\alpha V^2$). Besides, for AB@n-Si device, at higher injection levels (V > 0.6 V), the current transport transitions from a diode-like behavior to a SCLC regime, where the slope of the plot reaches ≈2.05. This confirms that the charge transport is governed by the Mott-Gurney law in the high-voltage region. The combined presence of recombination ($n = 1.57$) and SCLC (slope≈2) provides a complete physical picture of the carrier dynamics in the produced heterostructure [58, 59] A higher value of the ideality factor can also lead to a higher series resistance. The changes in series resistance (R_s) with voltage for both devices are shown in Fig. 3c. It can be seen that R_s decreases with increasing forward bias voltage. However, the R_s value of the AB@p-Si device is higher for every voltage value than AB@n-Si device. Because the width of depletion region is large at low forward bias voltages, a significant portion of the applied voltage is lost in this region, and the concentration of charge carriers contributing to conductivity in the neutral regions is low. Therefore, R_s is high. However, with increasing forward bias, the

width of depletion region narrows, increasing conductivity. This, in turn, reduces R_s. Shunt resistance (R_{sh}) is one of the important parasitic parameters in heterojunction diodes and plays an important role in leakage and device performance. A large R_{sh} indicates low leakage current paths. R_{sh}-V curves for both devices are given in Fig. 3d. It is seen that R_{sh} is high for both devices in reverse bias and partially increases with increasing bias. Since the width of the depletion region depends on the applied voltage, fluctuations in R_{sh} appear as a result of the capture and release of charge carriers by the traps between AB and Si with changing bias. Furthermore, R_{sh} increases abruptly for AB@p-Si in the zero-bias region, while it decreases conversely for AB@n-Si. In fact, because R_{sh} is an effective resistance that models the leakage paths in the diode, its value decreases when there is an open current path and increases when leakage currents are blocked.

By measuring a photodetector over a wide range of light intensities (P), we can obtain information about the device's thermal stability, sensitivity to light intensity, and the presence of internal gain. For this purpose, we performed I-V measurements over a wide range of white light intensities for both AB@n-Si and AB@p-Si devices. The photoresponse measurements were conducted by illuminating the device from the top (AB thin film side) to ensure that the incident photons directly interact with the AB@Si heterojunction interface. I-V measurements of AB@n-Si and AB@p-Si heterojunctions under varying white light intensities are given in Figs. 4a and b, respectively (The device schematic of the produced heterojunction devices is shown as an inset in Fig. 4c.). Measurements performed with a standard solar simulator (Sciencetech SF300 model (AM1.5 G)) show that both devices have a high photoresponse to white light, and the photoresponse even increases with increasing light intensity. This means that the number of photogenerated charge carriers increases proportionally to the light intensity, and the number of charge carriers that are drifted and collected at opposite ends increases with the reverse bias because of the enhanced electric field. However, when the currents of both devices are examined around zero bias, it is observed that the current of the AB@n-Si device is higher than that of the AB@p-Si device at all light intensities. This indicates that the internal electric field in the AB@n-Si device is higher than that in the AB@p-Si device, and that photogenerated carriers can be generated by this electric field when light is incident on the AB layer. Furthermore, although the reverse currents of both devices are close to each other, under illumination the reverse currents of AB@n-Si and AB@p-Si devices (at −2.0 V bias) are 3.10×10^{-6} and 6.01×10^{-7} A (for 10 mW/cm^2) and 1.40×10^{-4} and 1.14×10^{-4} A (150 mW/cm^2), respectively. Besides, in the forward bias region, the photocurrent is almost negligible since the width of the depletion region decreases with increasing bias [60]. Furthermore, the value of the photocurrent, which is already quite low relative to the forward current, may contribute to the forward current to a negligible extent due to the effect of recombination currents. This situation has been observed in our devices.

The curves of photocurrent (I_{ph}) versus bias voltage depending on light intensity are shown in Fig. 5a and b. It is clearly seen that the photocurrent increases with increasing light intensity for both devices. While the AB@n-Si heterojunction shows a partial increase in photocurrent with increasing bias voltage, the AB@p-Si heterojunction first exhibits a linear increase in photocurrent with increasing bias, followed by a saturation trend. This means that at high voltages, almost all photogenerated charge carriers are collected. Partial changes in both figures express the non-homogeneous interface structure between AB and Si and the trapping or release of charge carriers by the traps originating from them.

In most photodetector applications, such as image sensors and light meters, measurements can be taken across a wide range of light intensities to determine whether the photodetector has a constant photosensitivity. For this purpose, I-V measurements dependent on light intensity are important. The I_{ph} vs. V plots at constant bias voltage for both AB@n-Si and AB@p-Si heterojunction devices are shown in Fig. 5c and d, respectively. In general, it is observed that I_{ph} increases linearly with increasing light intensity for both devices. By linearly fitting the data, we found that the R-squared (coefficient of determination) of the linear fitting for AB@n-Si and AB@p-Si heterojunction devices are 0.977271 and 0.91583, respectively, which are indicating the linearity of the data [61]. For Fig. 5c and d, we obtained slopes of 1.74 and 1.68 for AB@n-Si and AB@p-Si, respectively, using the simple power law $I_{ph}=AP^c$. (Here, A, P and c are the proportionality constant, the light intensity incident on the device and the experimental coefficient, respectively). A slope greater than 1 also indicates the presence of internal gain in both devices. The c values for the same devices are 1.06×10^{-8} and 4.30×10^{-9}, respectively. Small c values indicate that the traps act as recombination centers, and the similar results in both A and c generally indicate that both devices operate with a similar mechanism [62]. The imperfect linear change (Fig. 5d) was attributed to the trapping of charge carriers, distributed within the energy gap [63]. Deviations from linearity may also occur due to traps caused by inhomogeneities or defective interface structures in the SiO_2 layer or between AB and Si [60]. In addition, the more pronounced linearity in AB@n-Si indicates that recombination losses in this device are lower than AB@p-Si.

A measure of a photodetector's response to light is the ON/OFF ratio, given by the ratio of the photocurrent under

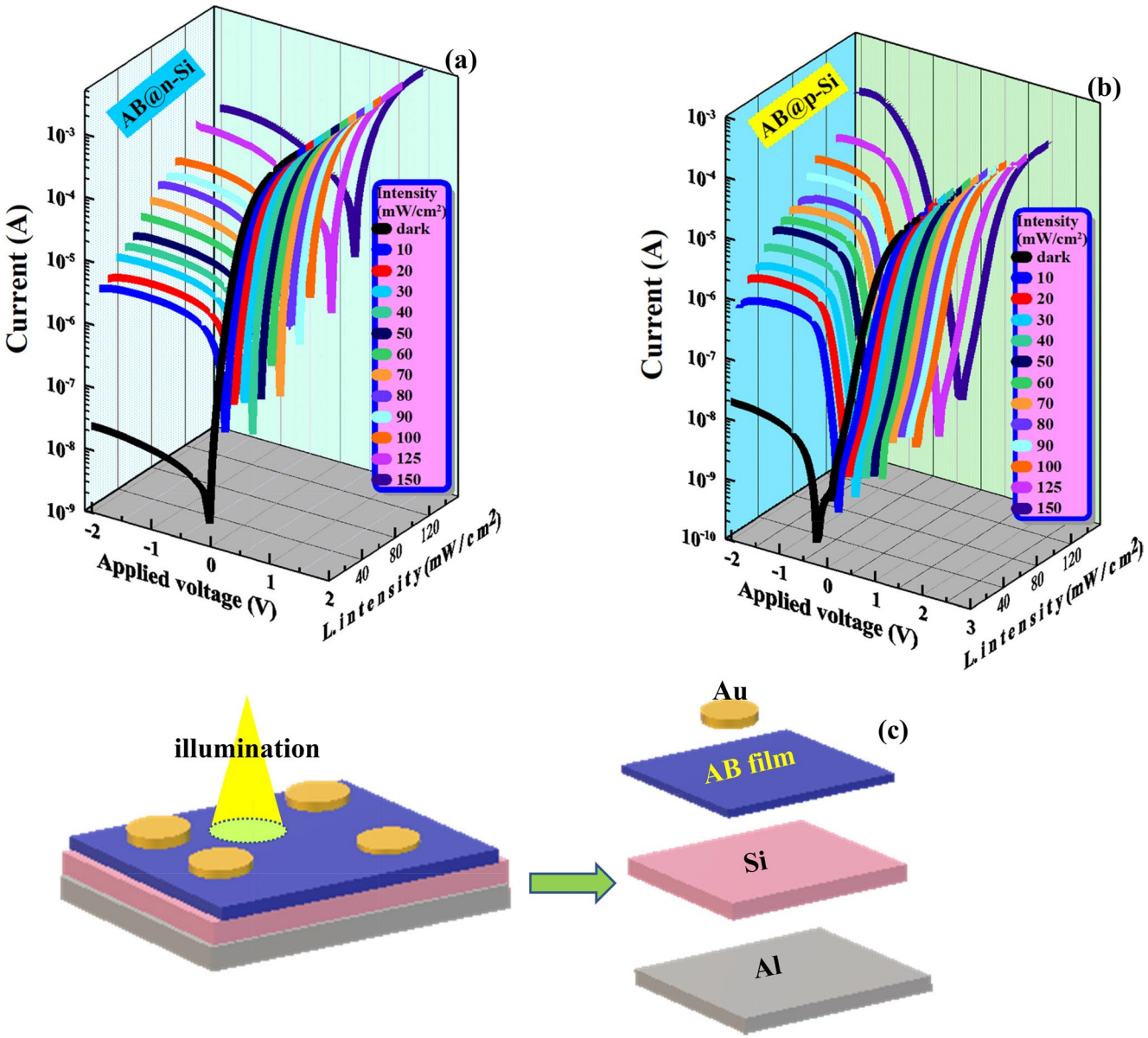

Fig. 4 (**a**) I-V measurements of AB@n-Si heterojunction dependent on white light intensity, (**b**) I-V curves for AB@p-Si device and (**c**) Device architecture

light to the dark current. That is, when the dark current is low and the photocurrent is high, this ratio will also be large. The ON/OFF ratio-V graphs as a function of light intensity for AB@n-Si and AB@p-Si devices are illustrated in Fig. 6a and b, respectively. While the change in the ON/OFF ratio with voltage is weak for the AB@n-Si device, it clearly increases with increasing light intensity. In the AB@p-Si device, in addition to the increasing ON/OFF ratio with increasing light intensity, both increasing and decreasing ON/OFF ratios depending on voltage are clearly observed. In AB@n-Si device, the increase in photocurrent with increasing light intensity increases the ON/OFF ratio, while in AB@p-Si device, the weak increase in photocurrent with voltage at low intensities and the more pronounced increase at high light intensities are the reasons for these behaviors. Additionally, it is clearly seen that the ON/OFF ratio peaks at this bias as a result of the low dark current at zero bias for both devices. For AB@n-Si, the highest ON/OFF ratio is 8396 at zero bias of 150 mW/cm^2, while for AB@p-Si, the highest value is calculated as 6578 at −1.78 V bias voltage of the same light intensity value.

Two of the most important parameters that measure the performance of photodetectors are responsivity (R) and detectivity (D). R is used to find the gain in electrical output

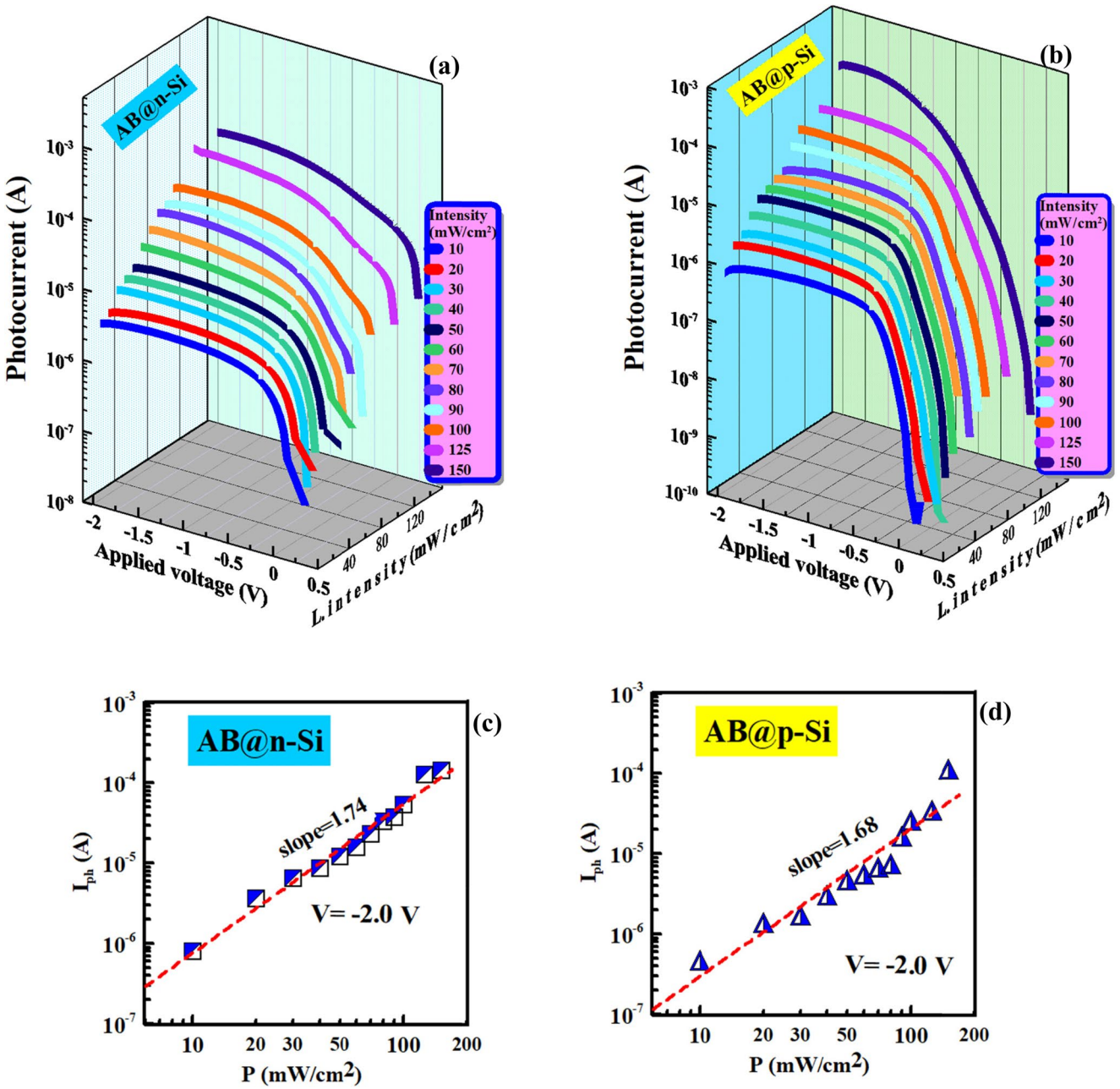

Fig. 5 Photocurrent-voltage graphs as a function of white light intensity: (**a**) for AB@n-Si and (**b**) for AB@p-Si device. Photocurrent-light intensity graph under a constant applied bias (**c**) for AB@n-Si and (**d**) for AB@p-Si heterojunction device

per optical input. In contrast, D indicates the photodetector's ability to measure weak optical signals that are distinguishable from noise. R and D are calculated using the following equations [64]:

$$R = \frac{I_{ph}}{PA} \tag{1}$$

$$D = R\sqrt{\frac{I_{ph}}{2qI_{dark}}} \tag{2}$$

where $I_{ph,}$ P, A and q indicate the photocurrent, illumination power, effective device area and electronic charge, respectively. Figs. 7a and b depict the R-V plots as a function of the light intensity. It is clear that the R values of both devices exhibit a non-linear change depending on voltage and light intensity. However, it is also seen that the dependence on intensity is more pronounced at high light intensities. In general, the AB@n-Si device exhibits higher R values than the AB@p-Si device across the entire light intensity range. For example, at the highest light intensity of 150 mW/cm^2

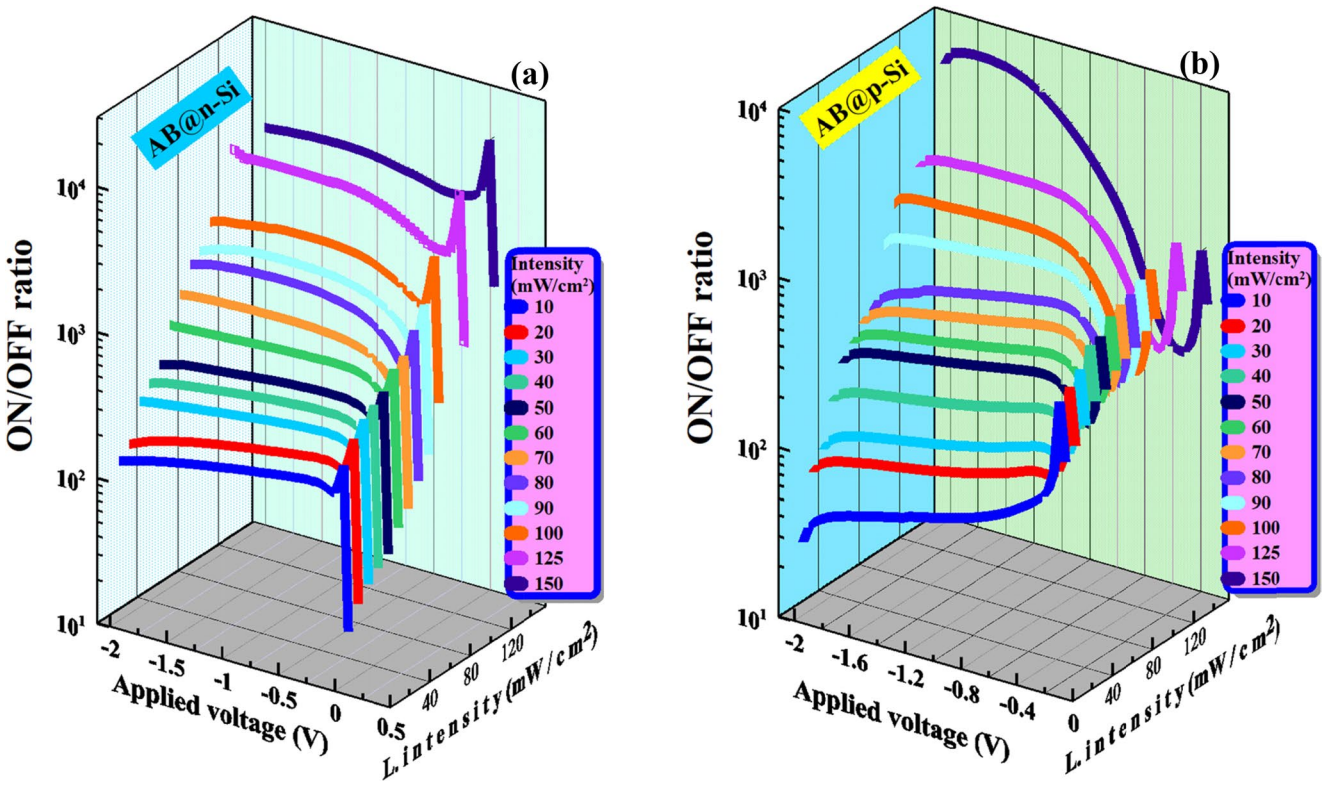

Fig. 6 ON/OFF ratio versus bias voltage (**a**) for AB@n-Si and (**b**) for AB@p-Si

and −2.0 Volts, the R values for the AB@n-Si and AB@p-Si devices were calculated as 123 and 97 mA/W, respectively. Peak values are observed just before −2.0 volts in both graphs. The drops following this peak value were attributed to recombination due to the effect of interface traps between AB and Si. Another reason for this decrease may be that photogenerated charge carriers, which gain high energy due to high electric fields or reverse bias voltage, reduce the total charge density as a result of colliding with each other [65, 66]. For both devices, the changes in D's light intensity and voltage showed behavior similar to R (Fig. 7c-d), and the highest D values were obtained at high light intensity and high bias voltage. For example, for a bias value of −2.0 volts at 150 mW/cm^2, the optimum values for AB@n-Si and AB@p-Si devices were obtained as 3.92×10^{10} and 3.20×10^{10} Jones, respectively. However, for the −2.0 V bias and at 10 mW/cm^2, for AB@n-Si and AB@p-Si devices, D were calculated as 6.09×10^9 and 2.47×10^9 Jones, respectively. The changes of the basic parameters R and D depending on the light intensity are given in Table 2 for both AB@n-Si and AB@p-Si photodetectors.

The I-V characteristics of AB@n-Si and AB@p-Si devices under light sources with four different wavelengths are shown in Fig. 8a and b, respectively. For both devices, the photoresponse is quite high across all wavelengths. Furthermore, while the rectification ratio is high for the AB@n-Si device with respect to AB@p-Si, the AB@p-Si device exhibits an I-V change that is close to ohmic behavior under light, i.e., a very low rectification ratio. In fact, it can be understood from the difference in reverse currents under dark and light conditions that the responses of both devices to light at different wavelengths are of the same order. However, it is observed that the photoresponse of the AB@n-Si photodetector increases with voltage up to 0.4 volts and does not change significantly with light wavelength. This indicates that the AB@p-Si device does not generate electron-hole pairs up to 0.4 V bias with light, and that the charge carriers are generated by an electric field corresponding to the sum of the external bias and the internal electric field (in depletion region). Following this voltage, wavelength-dependent changes are observed due to the photogenerated current caused by charge carriers originating from band-to-band of AB and Si or interfacial traps or from the functional groups of AB for different wavelengths. Furthermore, it can be seen from the I-V characteristics that both devices exhibit self-powered properties. The open-circuit voltage for the AB@n-Si and AB@p-Si devices was obtained as 0.20 and 0.35 V, respectively. In the AB@p-Si device, the permanent charge accumulation caused by charge traps at the interface has increased the internal electric field, leading to easy charge transfer. In this case, as shown in Fig. 8b, the early forward current has shifted slightly to the left

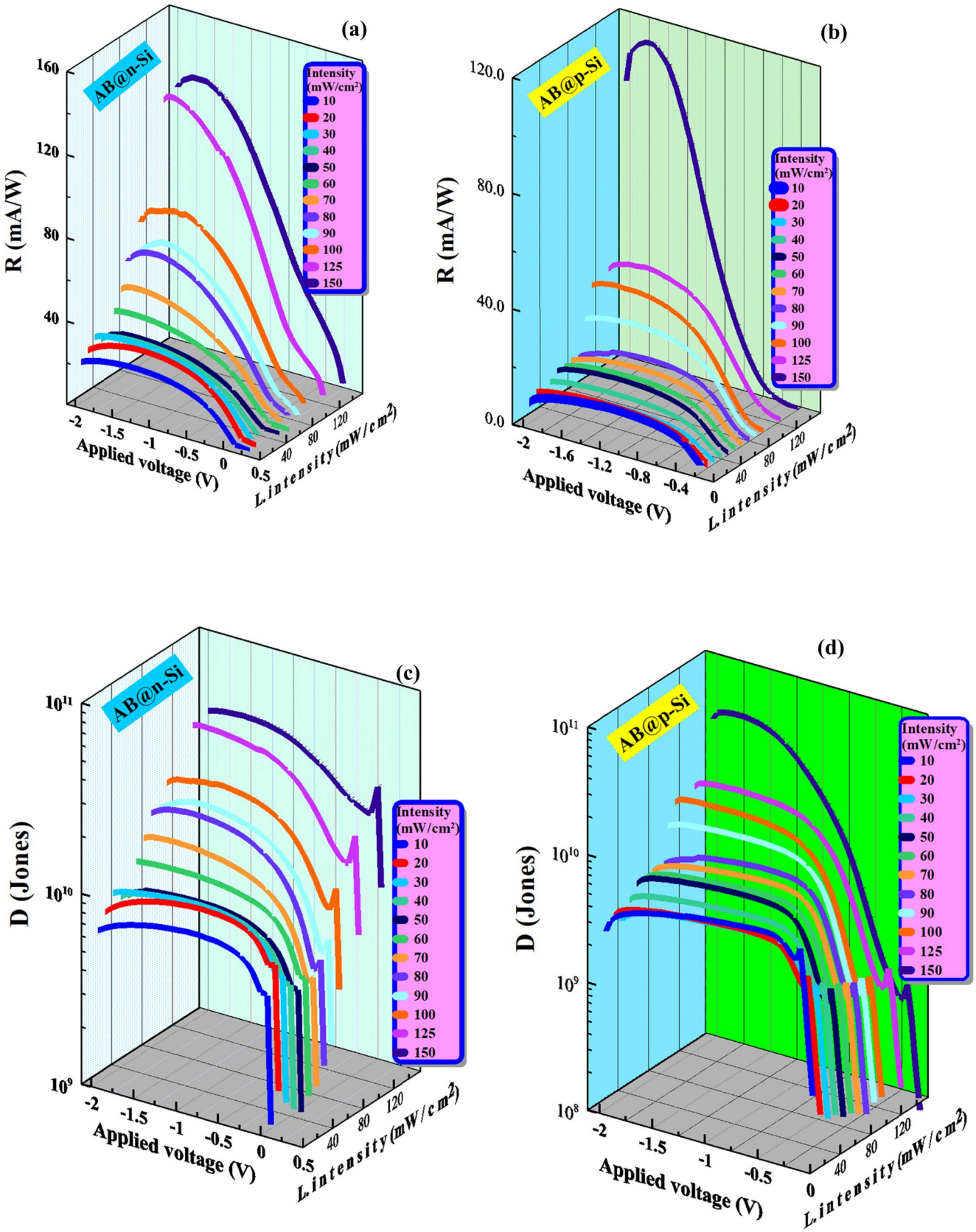

Fig. 7 R-V graphs as a function of white light intensity; (**a**) for AB@n-Si and (**b**) for AB@p-Si heterojunction device, D-V graphs; (**c**) for AB@n-Si and (**d**) for AB@p-Si heterojunction device

Table 2 Photodetector parameters of AB@n-Si and AB@p-Si heterojunctions for various light power densities (P) (at V= −2.0 V)

P (mW/cm^2)	AB@*n*-Si		AB@*p*-Si	
	R (mA/W)	D (Jones)	R (mA/W)	D (Jones)
10	19.77	6.32×10^{9}	7.37	2.48×10^{9}
20	23.23	7.40×10^{9}	8.91	2.99×10^{9}
30	27.52	8.77×10^{9}	7.41	2.49×10^{9}
40	24.55	7.82×10^{9}	9.81	3.30×10^{9}
50	23.79	7.58×10^{9}	12.09	4.06×10^{9}
60	33.90	1.08×10^{10}	11.99	4.03×10^{9}
70	42.13	1.34×10^{10}	12.41	4.17×10^{9}
80	53.68	1.71×10^{10}	11.92	4.01×10^{9}
90	53.01	1.69×10^{10}	23.74	7.98×10^{9}
100	68.34	2.38×10^{10}	33.84	1.14×10^{10}
125	131.06	4.10×10^{10}	35.61	1.21×10^{10}
150	123.12	3.92×10^{10}	96.80	3.26×10^{10}

of the I-axis. However, the wavelength-dependent reverse current of the AB@n-Si photodetector is relatively high at 590 and 365 nm compared to other wavelengths. Similarly, for the AB@p-Si photodetector, higher reverse current is observed at 590 and 365 nm compared to other wavelengths in wavelength-dependent changes beyond 0.4 volts. This situation was attributed to lower light absorption and photogenerated charge carrier formation in AB@n-Si due to Si, which has a band gap of 1.12 eV at 850 nm in both devices. However, it can also be explained by higher light absorption and photogenerated charge carrier formation at 590 nm due to the interface energy states and at 365 nm in the AB layer [67]. The higher photoresponse at 365 nm UV light originates from the AB layer, and it is understood that at 365 nm, the release of electrons trapped in defects at the AB/Si interface is effective, rather than direct band-to-band electron transfer from the AB layer. It is observed that the photoresponse for both devices are close to each other, and electron-hole pairs are formed even at very low bias voltages for AB@p-Si due to a higher bias voltage (or built-in electrical field). In addition, it is clearly seen that AB@n-Si also responds to light after a certain voltage, just like in the I-V graphs (Fig. 8c and d). The high photocurrent at 590 nm for both devices was attributed to charge carriers emitted

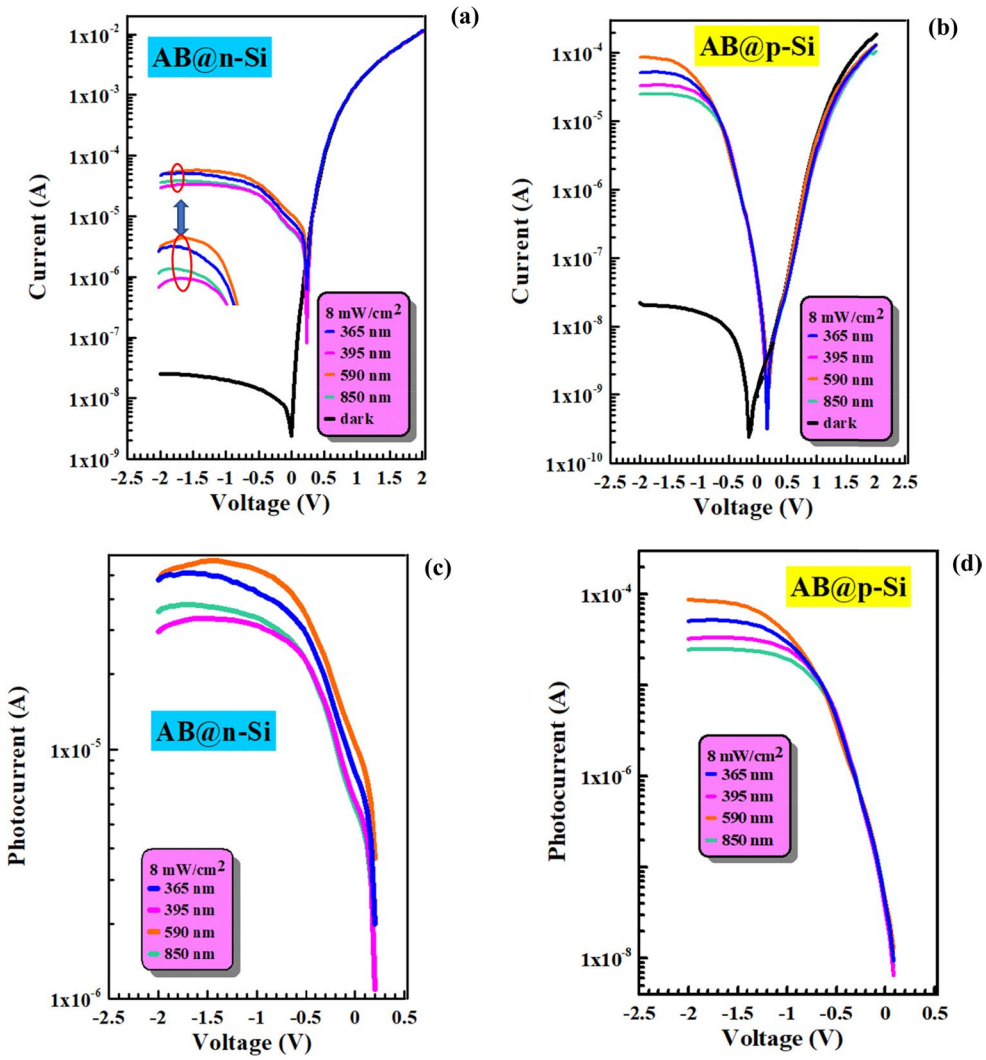

Fig. 8 Comparison of I-V measurements performed at different wavelengths with 8 mW/cm^2 light intensity with those in dark current (**a**) for AB@n-Si and (**b**) AB@p-Si heterojunction. Wavelength-dependent photocurrent-bias voltage graphs (**c**) for AB@n-Si and (**d**) AB@p-Si heterojunction

as a result of photon absorption through defects/tail states formed between AB and Si at this wavelength and local levels within the energy band gap [68].

ON/OFF ratio-voltage graphs for different wavelengths are shown in Fig. 9a and b. It is clearly seen that the ON/OFF ratios of both photodetectors vary with both bias and wavelength. While the AB@n-Si device has the highest ON/OFF ratio at zero bias, the highest values for AB@p-Si are more clearly seen at higher voltage values. As mentioned above, in the AB@p-Si photodetector, the current is generated by bias voltage (or built-in electrical field) up to a certain voltage, and then by the effect of light. That is, at low biases, the current is generated by the electric field, and since the current around zero bias is close to the current in dark, the ON/OFF ratio around zero bias is lower than that of AB@n-Si. According to the measurement results at all wavelengths, the highest ON/OFF ratios for both devices were obtained at 590 nm. Specifically, the highest ratio for AB@n-Si at zero bias was calculated as 4375, while for AB@p-Si it was 4237 at −1.88 V.

The R-V graphs calculated using Eq. 1 based on wavelength are depicted in Fig. 10a and b. In accordance with the photoelectric effect, the highest values of R for both devices were obtained at 590 nm. For example, at 590 nm, the highest value for AB@n-Si was calculated as 906 mA/W (for −1.4 V), while for AB@p-Si it was 1384 mA/W (for −2.0 V). For the AB@n-Si device, the decrease in R after its maximum value was attributed to trap-assisted recombination processes. The different values and different responses in both devices depending on the wavelength can be explained by the different interface structures of both devices and the resulting different activation energies of the traps in the interface defect and energy states formed between AB and Si.

The performance parameters of the wavelength-dependent photodetector are given in Table 3 at V= −2.0 V.

The external quantum efficiency (EQE) of a photodetector is a fundamental performance metric that indicates the detector's efficiency in converting incident photons into electrical carriers (electron-hole pairs). The EQE of a photodetector can be calculated according to the expression [69]:

$$EQE = R\frac{hc}{q\lambda} \tag{3}$$

where, R, h, c, λ and q are responsivity, Planck's constant, speed of light, wavelength of the light, and elementary charge, respectively. Plots of EQE versus voltage calculated using Eq. 3 for AB@n-Si and AB@p-Si heterojunction photodetectors under different wavelengths are given in Fig. 11a and b, respectively. It is clearly seen that EQE varies with both wavelength and voltage. Furthermore, the highest EQE value for the AB@n-Si device is observed under 365 nm UV light, while the lowest is observed under 850 nm IR light. For example, the optimum EQE value is 267(%) under 365 nm light (at −1.76 V), while it is 85(%) (at −1.68 V), at 850 nm. After these values, the partial decrease in EQE with increasing voltage is attributed to the recombination of charge carriers by traps due to the inhomogeneous interface structure [25, 57]. For the AB@p-Si photodetector, the highest EQE values were obtained at 590 and 365 nm, while the lowest value was obtained at 850 nm. The optimum EQE values at 590 and 365 nm were obtained as 282(%) (for − 2.0 V) and 274(%) (for − 1.72 V), respectively. The highest EQE value at 850 nm was obtained as ~56(%) at −2.0 volts. The overall evaluation of the EQE values for both devices shows that the EQE exceeds 100% at wavelengths other than 850 nm. This high value of EQE

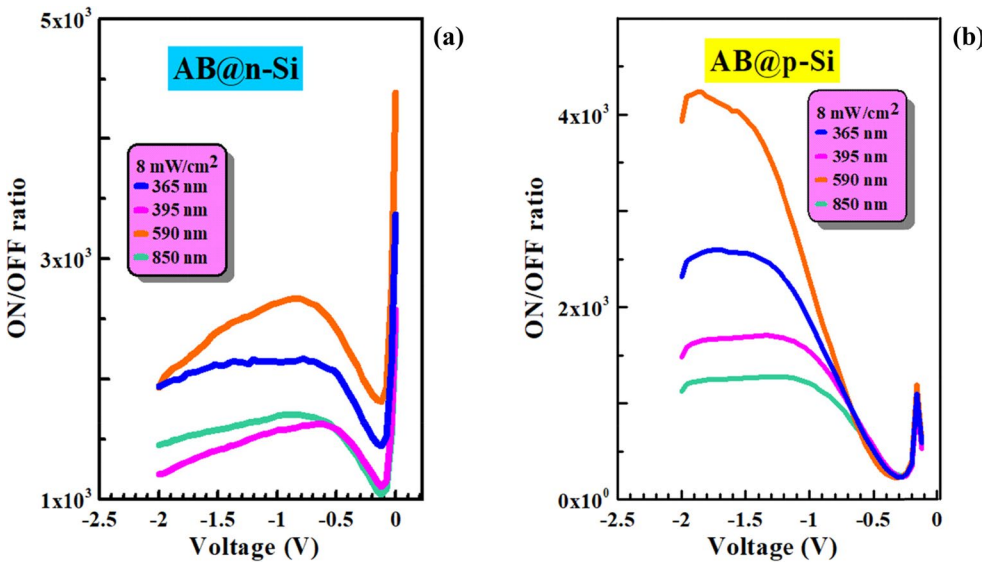

Fig. 9 (**a**) ON/OFF ratio versus bias voltage graphs as a function of wavelength (**a**) for AB@n-Si and (**b**) AB@p-Si heterojunction

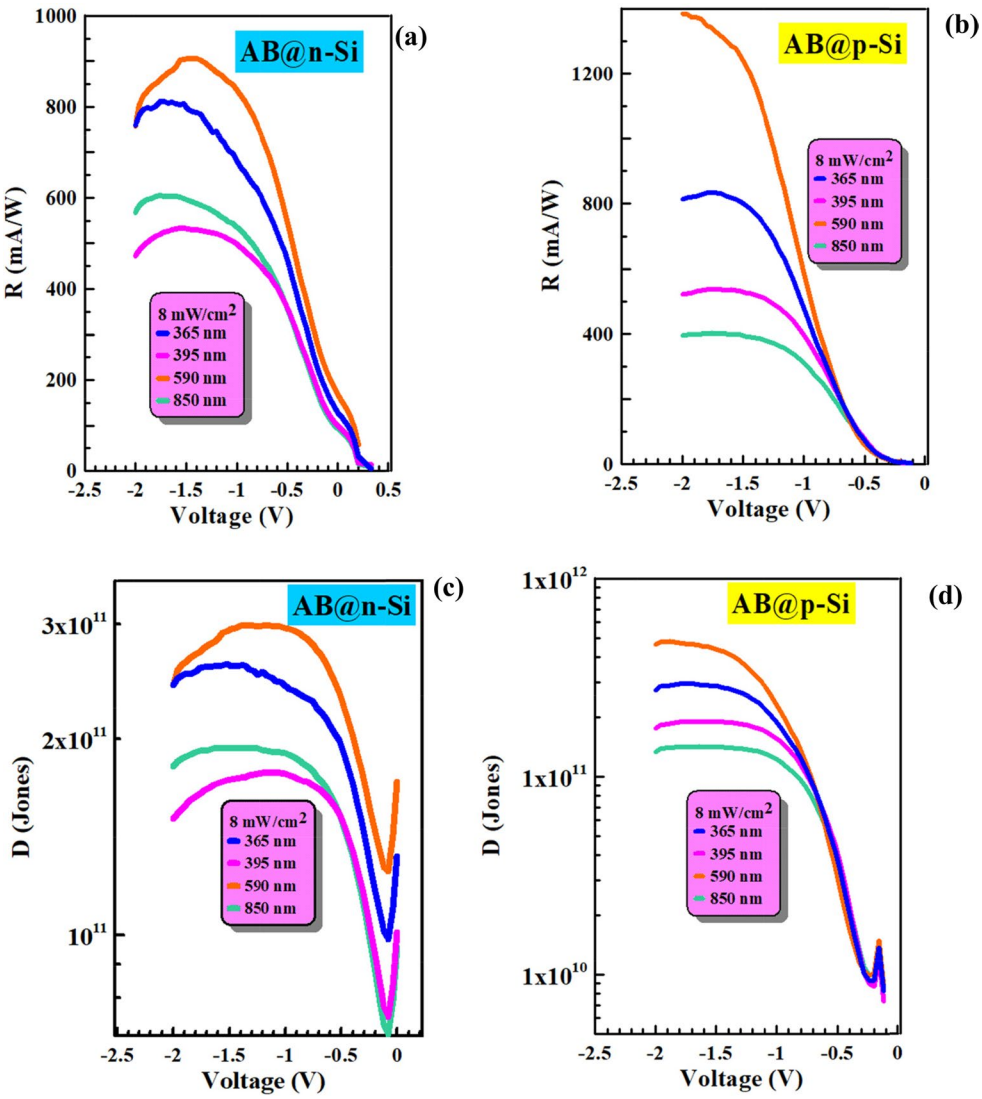

Fig. 10 (**a-b**) R-V plots as a function of wavelength and (**c-d**) D-V plots for AB@n-Si and AB@p-Si heterojunction devices

Table 3 Photodetector parameters of AB@n-Si and AB@p-Si heterojunctions for different wavelength (λ) (at V= −2.0 V)

λ (nm)	AB@*n*-Si (V= −2.0 V)			AB@*p*-Si(V= −2.0 V)		
	R (mA/W)	D (Jones)	EQE(%)	*R* (mA/W)	D (Jones)	EQE(%)
365	749	2.42×10^{11}	250	814	2.73×10^{11}	268
395	473	1.51×10^{11}	143	520	1.74×10^{11}	159
590	758	2.42×10^{11}	154	1384	4.66×10^{11}	282
850	569	1.82×10^{11}	80	394	1.32×10^{11}	56

is attributed to the high photoresponse under UV light in the AB layer and the contribution to the photocurrent by the discharge of interfacial traps at different wavelengths, resulting in a photoconductivity gain for the devices at these wavelengths [70]. Furthermore, the remarkably high EQE values (exceeding the unity limit) indicate that the device operates in a photomultiplication regime. We attribute this performance to the impact ionization mechanism within the AB@Si, where the accelerated primary photo-generated carriers gain sufficient kinetic energy to impact the lattice and generate additional carriers, thereby significantly enhancing the device's responsivity [71–73].

Energy-band diagrams illustrating the photocurrent generation mechanism in the devices are shown in Fig. 11c and d. When p-type AB and n-Si materials, whose p-type status has been determined by comparison with a p-type reference material, are combined, electrons flow from the n-Si side toward the p-AB side until the Fermi levels of both materials are equalized. At equilibrium, the equilibrium E_F level shown in Fig. 11c is reached. These electron transitions

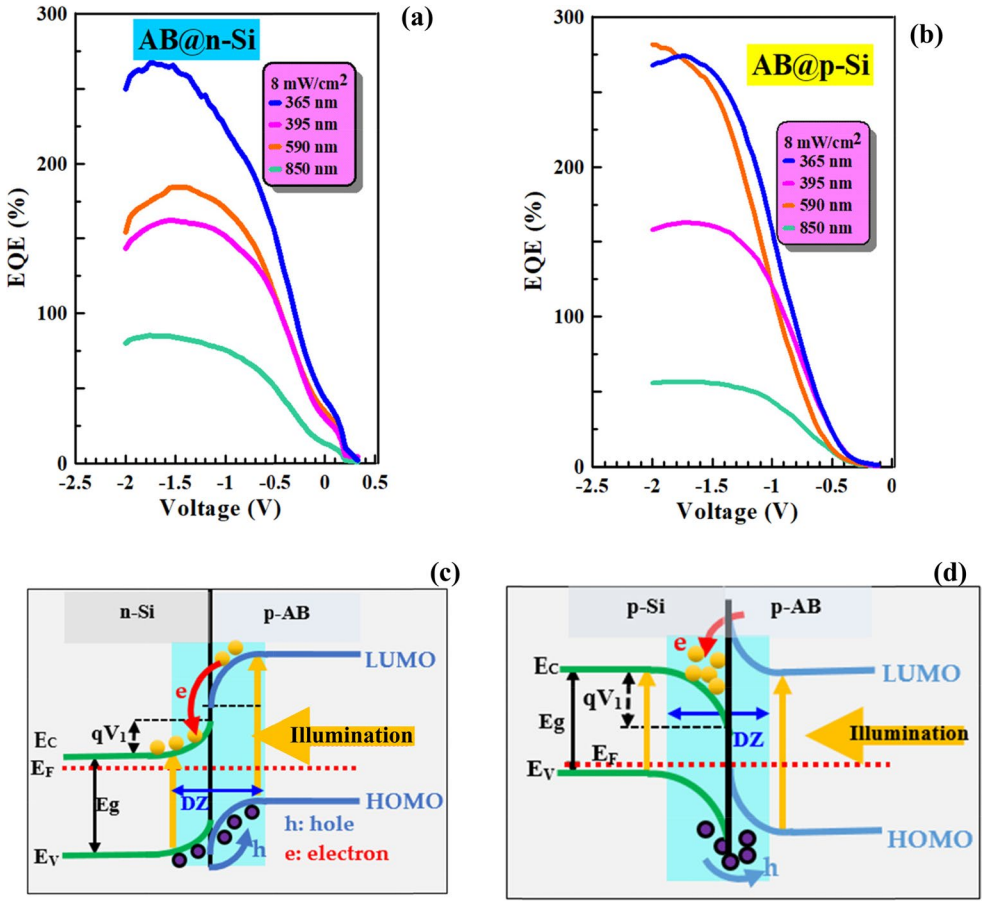

Fig. 11 EQE-V plots as a function of wavelength (**a**) for AB@n-Si, (**b**) AB@p-Si heterojunction device; energy-band diagrams illustrating the photocurrent generation mechanism in devices for (**c**) AB@n-Si and (**d**) AB@p-Si

cause band bending in the region indicated by the depletion zone (DZ) in both materials, and an internal (built-in) electric field forms in this region from right to left. At low forward bias voltages, current is generated as carriers overcome the potential barrier (thermionic emission). However, the fact that the ideality factor is greater than 1 (1.57) indicates that interface recombination is active. In other words, while some electrons and holes overcome the barrier, others recombine at defect levels at the interface. Deep traps within the organic layer (AB) and at the interface are filled by the injected carriers. During this process, the current responds very sharply to even small increases in voltage. A low reverse bias current is generated in the dark.

Under IR light, high-energy photons generate carriers in the Si surface. They also excite electrons trapped in the interface ("de-trapping") and incorporate them into the current (photoconductive gain). Light at 590nm (visible) passes through the organic layer and reaches deep into the Si depletion region. The electron-hole pairs formed here are rapidly separated by the internal electric field. The AB layer acts as an effective passivation agent in this region, reducing surface recombination and maximizing efficiency (EQE). Furthermore, when light (UV or visible) strikes the material, electron-hole pairs are generated. Under these conditions, the internal electric field and the electric field caused by the external bias are in the same direction. Therefore, the electron-hole pairs generated by the light effect separate, with the electrons moving toward the n-Si layer and the holes moving toward the p-Si layer, eventually reaching the electrodes.

When AB and p-Si are brought together, electrons flow from AB to p-Si and holes flow from p-Si to AB, reaching equilibrium conditions and forming a depletion region. At equilibrium, an internal electric field develops from right to left (Fig. 11d). The barrier in the region where the bends between the two materials occur acts as an accumulation zone for the carriers. Under the forward bias, the holes moving from p-Si to AB must pass through this barrier region. When light strikes the AB layer under reverse bias, electrons excited by UV light are transferred very rapidly from the LUMO level of the AB to the conduction band (CB) of p-Si and a portion of the light-induced carriers are trapped in the traps at the interface. This trapping modulates the local electric field at the interface. As long as a trapped charge remains there, a large number of opposite charges are injected into the device from the external circuit to maintain charge balance. The photogenerated carrier density can also increase when UV photons have sufficient

energy to excite carriers trapped in deep trap levels at the interface. Interface traps multiply the current by extending the lifetime of the photoconductors. This is the "photoconductive gain" mechanism, which causes multiple electrons to flow from a single photon.

The device exhibits a distinct wavelength-dependent photoresponse, rooted in different physical processes. The high responsivity at **365 nm** is attributed to the UV-induced de-trapping of carriers from interface states, leading to a photoconductive gain mechanism. In contrast, the peak performance at **590 nm** originates from the optimized collection of carriers generated deep within the Si depletion region. At this wavelength, the *Alcea biennis* layer serves a dual purpose: it provides effective surface passivation to minimize recombination losses and functions as a hole-selective interlayer.

A comparison of the AB@Si photodetector's instrument performance with other previously reported organic/inorganic hybrid and silicon-based heterojunction photodetectors is given in Table 4.

The exceptional optoelectronic response of the AB@Si hybrid photodetector can be attributed to the synergistic effects of its phenolic constituents and essential elements identified in the aqueous extract. Phenolic compounds such as tiliroside, kaempferol derivatives, and flavonoid glycosides possess extended π-conjugation and abundant hydroxyl and carbonyl groups that facilitate strong electronic coupling and efficient charge transfer at the semiconductor interface, thereby enhancing photoresponsivity and broadening spectral absorption. Similar findings were reported in studies on plant-based photodiodes employing anthocyanin- and flavonoid-sensitized junctions, where phenolic π-systems enabled visible-to-NIR sensitization and improved built-in electric field strength across the hybrid interface.

In addition, the elemental composition of *AB*, dominated by K, Mg, Ca, and Zn, supports the formation of interfacial dipoles and defect passivation layers. These elements are known to influence surface potential and dielectric balance in bio-hybrid materials—potassium enhancing ionic mobility and conductivity, magnesium and calcium contributing to charge neutrality and film stability, and zinc facilitating exciton dissociation and electron transport through coordination with oxygen-rich phenolic sites. Consequently, the AB layer likely operates through (i) spectral complementarity between phenolic chromophores and the underlying semiconductor to expand the detection range, (ii) element-assisted dipole formation that strengthens the built-in potential enabling self-driven operation, and (iii) phenolic–metal coordination networks that minimize interfacial traps and dark current.

One of the major problems that makes organic materials disadvantageous for practical optoelectronic applications is their inability to maintain stability over long periods of time. Therefore, stable organic materials are considered a step ahead in practice. For this purpose, the stability of the AB@n-Si heterojunction device, which was left in the atmospheric environment after device fabrication, was retested under different light sources 152 and 327 days after its fabrication to evaluate the performance of the AB pigment organic material both in the dark and under different light sources (Fig. 12a-d) (Since the stability of inorganic silicon is known, only time-dependent stability results for AB@n-Si were provided to observe the stability of the AB). As seen, the device is stable under all light sources used in both dark and experimental stages, maintaining its antisymmetric I-V characteristic. The fact that the reverse current does not change in the dark demonstrates that the device maintains its stable physical design. However, it was considered that the partial changes in the device's I-V measurements might

Table 4 Comparison of the optoelectronic performance parameters of the fabricated AB/n-Si photodetector with other reported organic/inorganic heterojunction devices in the literature

Device	λ(nm)	ON/OFF ratio	D* (Jones)	*R* (mA/W)	EQE (%)	Ref.
AB@n-Si	590	4375	2.42×10^{11}	758	154	**This work**
AB@p-Si	590	4237	4.66×10^{11}	1384	282	
Al/DPAVBi/n-Si	600	-	3.37×10^{10}	890	7.01	[74]
Gr/H–Gr/Si	532		2.3×10^{11}	245	**~60**	[75]
EA/n-Si	850	~2.5×10^{4}	1.41×10^{12}	650	149	[76]
graphene: PVA/p-Si	White	1.41×10^{4}	5.35×10^{9}	5.7×10^{-5}	-	[77]
DiMe-PTCDI/p-Si	IR	-	7.0×10^{7}	0.2	9×10^{-5}	[78]
BTPDS-8/Si	850	983	1.22×10^{10}	1.56	-	[79]
PEDOT: PSS/p-Si	455	-	2.85×10^{11}	527.5	~ 80	[80]
MDMO-PPV/n-Si	351–1100		8×10^{10}	2.2	0.5	[81]
PANI: Coronene/p-Si	white	-	3.94×10^{10}	5.34	-	[82]
CU/Si	395	1.8×10^{4}	1.22×10^{11}	13.19 A/W	4.51×10^{3}	[83]
PPD-RGO/Si	382	-	-	1.4	-	[84]
HBS/n-Si	850	~10^{5}	2.0×10^{10}	1160	-	[20]
LiPOM/p-Si	1000	-	4.34×10^{10}	64.17	7.96	[85]

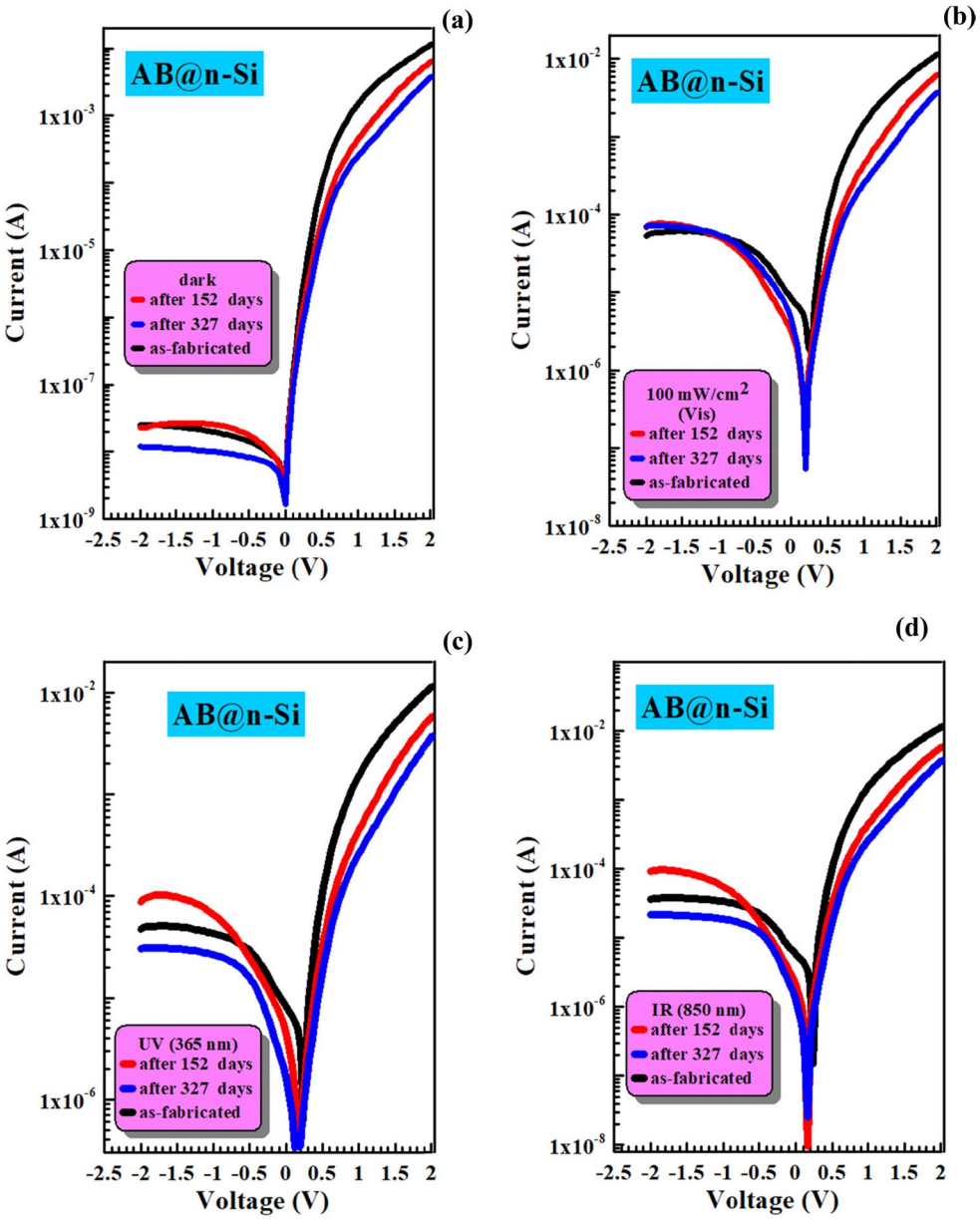

Fig. 12 I-V measurements showing the time-dependent stability tests of the AB@n-Si device (**a**) in the dark, (**b**) under 150 mW/cm2 Visible light, (**c**) under 365 nm and (**d**) under 850 nm illumination

have been caused by unstable derivatives resulting from the reaction between oxygen in the air and the AB surface. In other words, the partial improvement in photocurrents was attributed to the device's ability to increase conductivity in the AB layer by acting as a molecular dopant in the air environment, utilizing O_2 and H_2O in the air. Furthermore, the partial decrease observed in the forward current during the stability measurements can be attributed to the increase in series resistance induced by the interfacial oxidation of the silicon surface. Over the 205-day storage period, the formation of a thin native oxide layer (SiOx) at the heterojunction interface serves as an additional barrier for charge carrier transport, which slightly restricts the forward current flow [86].

4 Conclusion

In conclusion, novel type of organic/inorganic heterojunction photodetectors were fabricated by facile spin coating of an AB plant pigment layer on n-type and p-type Si to obtain AB@Silicon devices. Both devices exhibited excellent rectifying in the dark, with the forward current of AB@n-Si being higher than that of AB@p-Si, while the reverse currents were found to be close to each other. The difference in currents in the forward bias was explained by the non-homogeneous interface structure for AB@p-Si and the higher density of interface traps compared to AB@n-Si. It was seen that both hybrid photodetectors can operate without external bias. Additionally, both devices demonstrated high performance

under white light, UV, and IR light. Measurements based on white light intensity showed that the ON/OFF ratios in AB@n-Si and AB@p-Si devices could reach values of 8396 and 6578, respectively, for a light intensity of 150 mW/cm^2.

Under lights with an intensity of 8 mW/cm² and wavelengths of 365, 395, 590, and 850 nm, it was generally observed that the performance at 365 nm was higher than at the other wavelengths. This was attributed to the significant light absorption of the AB layer, which has a wider band gap than Si, leading to the formation of electron-hole pairs for UV light. For AB@n-Si, the R, D, and EQE values are 749 mA/W, 2.42×10^{11} Jones, and 250 (%), while for AB@p-Si, the same parameters reached 814 mA/W, 2.73×10^{11} Jones, and 268 (%) respectively.

Author Contributions All authors contributed equally to the writing of the work.

Funding Open access funding provided by the Scientific and Technological Research Council of Türkiye (TÜBİTAK). This research received no specific grant from funding agencies in the public, commercial, or not-for-profit sectors.

Data availability All data included in this paper are available upon request by contact with the corresponding author.

Declarations

Ethical approval This study does not involve human or animal subjects, and thus, no ethical approval is required. The study protocol adheres to the guidelines established by the journal.

Conflict of interest The authors declare that they have no known competing financial interests or personal relationships that could have appeared to influence the work reported in this paper.

References

1. K. Baeg, M. Binda, D. Natali, M. Caironi, Y. Noh, Adv. Mater. **25**, 4267 (2013)
2. Q. Lin, A. Armin, P.L. Burn, P. Meredith, Nat. Photonics **9**, 687 (2015)
3. X. Liu, D. Yu, F. Cao, X. Li, J. Ji, J. Chen, X. Song, H. Zeng, Small **13**, (2017)
4. C. Wang, X. Zhang, W. Hu, Chem. Soc. Rev. **49**, 653 (2020)
5. C.W. Joo, J. Kim, J. Moon, K.M. Lee, J.E. Pi, S.Y. Kang, S.D. Ahn, Y.S. Park, D.S. Chung, Org. Electron. **70**, 101–106 (2019)
6. A. Wadsworth, Z. Hamid, J. Kosco, N. Gasparini, I. McCulloch, Adv. Mater. **32**, 2001763 (2020)
7. X. Liu, Y. Lin, Y. Liao, J. Wu, Y. Zheng, J. Mater. Chem. C **6**, 3499–3513 (2018)
8. L. Xie, W. Song, J. Ge, B. Tang, X. Zhang, T. Wu, Z. Ge, Nano Energy. **82**, 105770 (2021)
9. Y. Xu, H. Yao, J. Hou, Chin. J. Chem. **37**, 207 (2019)
10. A. Armin, W. Li, O.J. Sandberg, Z. Xiao, L. Ding, J. Nelson, D. Neher, K. Vandewal, S. Shoaee, T. Wang, H. Ade, T. Heumüller, C. Brabec, P. Meredith, Adv. Energy Mater. **11**, 2003570 (2021)
11. S. Zeiske, W. Li, P. Meredith, A. Armin, O.J. Sandberg, Cell Rep. Phys. Sci. **3**, 101096 (2022)
12. Ç. Çetinkaya, E. Çokduygulular, B. Kınacı, F. Güzelçimen, İ Candan, H.İ Efkere, Y. Özen, S. Özçelik, Opt. Mater. **120**, 111457 (2021)
13. R.D. Jansen-van Vuuren, A. Armin, A.K. Pandey, P.L. Burn, P. Meredith, Adv. Mater. **28**, 4766 (2016)
14. S.-W. Jeon, H.-J. Choi, J.-H. Bae, B.-C. Kim, S.-W. Choi, J. Inf. Disp. **19**, 129 (2018)
15. X. Li, J. Wan, Y. Tang, C. Wang, Y. Zhang, D. Lv, M. Guo, Y. Ma, Y. Yang, ACS Appl. Mater. Interfaces. **16**, 29003 (2024)
16. S.M. Abed, S.M. Mohammad, A.A. Sifawa, Z. Hassan, M. Abdullah, H. Naser, J. Mater. Sci. Mater. Electron. **36**, 1858 (2025)
17. Q. Li, X. Li, L. Ding, Y. Li, J. Ma, S. Sang, T. Minami, ACS Appl. Electron. Mater. **7**, 6166 (2025)
18. C. Feng, W. Zhou, W. Li, H. Cheng, X. Fan, L. Xiao, B. Zhang, Opt. Mater. (Amst). **165**, 117110 (2025)
19. A. Ansari, S. Ahmed, M.H.J. Mashniwi, S.M. Shinde, A. Khan, P. Ranjan, D.S. Negi, J. Mater. Sci. **60**, 2711 (2025)
20. H. Yuca, S. Karakaya, F. Yıldırım, Ü. İncekara, Ş. Aydoğan, Phys. Scr. **98**, 125982 (2023)
21. K. Zhou, B. Qi, Z. Liu, X. Wang, Y. Sun, L. Zhang, Adv. Funct. Mater. **34**, 2411671 (2024)
22. A.A. Hussaini, M. Yıldırım, J. Mater. Sci. **60**, 16226 (2025)
23. F. Yıldırım, Z. Orhan, Ş Aydoğan, Mater. Res. Bull. **159**, 112113 (2023)
24. A.A. Hussaini, M. Yıldırım, Sens. Actuators A Phys. **389**, 116545 (2025)
25. K. Ganjehyan, F. Yıldırım, M. Erdoğan, S. Nuhzat, A. Daştan, Ş Aydoğan, Mater. Today Energy **51**, 101886 (2025)
26. F. Yıldırım, S. Karakaya, H. Yuca, H. Ertap, M. Karabulut, Ş. Aydoğan, ACS Appl. Electron. Mater. **7**, 4881 (2025)
27. M. Peymannia, K. Gharanjig, A.M. Arabi, Int. J. Energy Res. **44**, 309 (2020)
28. A.L. Öztürk, F. Babaoğlu, S. Uzunhisarcikli, M E V M G I S Adv. Mol. Biol. **1**, 47 (2009)
29. J. Lee, D. Lee, D. Jeong, N. Park, Adv. Funct. Mater. **29**, 1807047 (2019)
30. G. Murali, A. Thakur, S. Dixit, S. Singh, A. Stefańska, Sustain. Mater. Technol. **45**, e01628 (2025)
31. L. Chen, Y. Zhang, Z. Chen, Y. Dong, Y. Jiang, J. Hua, Y. Liu, A.I. Osman, M. Farghali, L. Huang, D.W. Rooney, P.-S. Yap, Environ. Chem. Lett. **22**, 715 (2024)
32. G. Calogero, J.-H. Yum, A. Sinopoli, G. Di Marco, M. Grätzel, M.K. Nazeeruddin, Sol. Energy **86**, 1563 (2012)
33. G. Richhariya, A. Kumar, P. Tekasakul, B. Gupta, Renew. Sustain. Energy Rev. **69**, 705 (2017)
34. M. Dhorkule, P. Lamrood, S. Ralegankar, S.P. Patole, S.S. Wagh, H.M. Pathan, ES Food Agrofor. **16**, 1086 (2024)
35. Z. Azadeh, K. Saeidi, Z. Lorigooini, M. Kiani, F. Maggi, SN Appl. Sci. **2**, 927 (2020)
36. B. Sharifi, K. Saeidi, B. Shiran, E. Shahbazi, Z. Lorigooini, M. Rahimifard, Ind. Crops Prod. **220**, 119275 (2024)

37. M. Pakravan, H. Abedinzade, J. Safaeepur, Pak. J. Biol. Sci. **10**, 2603 (2007)
38. R.B. Ozturk, G. Zengin, K.I. Sinan, D. Montesano, D. Zheleva-Dimitrova, R. Gevrenova, A.I. Uba, U. Çakılcıoğlu, A. Kaplan, S. Jugreet, S. Dall'Acqua, M.F. Mahomoodally, Molecules. **27**, 5011 (2022)
39. H.R. Bajes, S.A. Oran, Y.K. Bustanji, Res. J. Pharm. Technol. **14**, 6447 (2021)
40. F.S. Mohammed, M. Sevindik, I. Uysal, E. Sevindik, H. Akgül, Biol. Bull. **49**, S59 (2022)
41. M. Castillo-Carrión, R. Martínez-Espinosa, J.Á. Pérez-Álvarez, J. Fernández-López, M. Viuda-Martos, R. Lucas-González, Foods **13**, 237 (2024)
42. G.J. Mir, B. Ahmad Dar, S.A. Ganie, R. Hamid, INNOSC Theranostics Pharmacol. Sci. **8**, 62 (2025)
43. N.K. Khidyrova, S.M. Turaeva, M.J. Rakhmatova, K.M. Bobakulov, S.S. Sagdullaev, R.P. Zakirova, K.U. Khodjaniyazov, K. Torikai, ACS Omega. **7**, 19892 (2022)
44. J. Liao, Y. Luo, H. Yang, W. Deng, J. Bai, Y. Pan, B. Jiang, Y. Jia, Front. Plant. Sci. **17**, 1778764 (2026)
45. H.C. Olcay, A. Dogan, A. Battal, T. Yaman, M.A. Yılmaz, S.M. Pınar, O. Cakir, Fitoterapia. **187**, 106933 (2025)
46. M. Najaflu, M. Shahgolzari, F. Bani, A.Y. Khosroushahi, ACS Omega. **7**, 34573 (2022)
47. S. Karakaya, M. Koca, O. Sytar, B. Dursunoglu, H. Ozbek, H. Duman, Z. Guvenalp, C.S. Kılıc, South. Afr. J. Bot. **121**, 536 (2019)
48. S. Öner, A. Kadı, E. Tekman, A.C. Kararenk, E.B. Özer, K.N. Ergin, H. Yuca, M.E. Arslan, R. Duman, A.A. Şahin, N.M. Pinar, A. Atila, G.E. Bona, S. Karakaya, Protoplasma. **262**, 857 (2025)
49. Ş. Aydoğan, M. Sağlam, A. Türüt, Microelectron. Reliab. **52**, 1362–1366 (2012)
50. M. Zhang, J. Zhao, X. Dai, X. Li, Separations. **10**, 598 (2023)
51. M.M. Ramesh, N.S. Shankar, A.H. Venkatappa, Pharmacogn Rev. **18**, 68 (2024)
52. R.J.C. Brown, M.J.T. Milton, TrAC Trends Anal. Chem. **24**, 266 (2005)
53. E.H. Rhoderick, R.H. Williams, *Metal-Semiconductor Contacts* (Clarendon, 1988)
54. A. Kocyigit, M. Yılmaz, Ş. Aydoğan, Ü. İncekara, J. Alloys Compd. **790**, 388–396 (2019)
55. M. Yilmaz, C. Cirak, N. Canpolat, S. Aydogan, Appl. Phys. A **129**, 224 (2023)
56. A. Karaca, D.E. Yıldız, A.A. Hussaini, M. Yavuz, M. Yıldırım, D.A. Köse, J. Mater. Sci. Mater. Electron. **37**, 266 (2026)
57. B.C. Şakar, F. Yıldırım, E. Şakar, Ş. Aydoğan, J. Phys. D Appl. Phys. **58**, 245105 (2025)
58. Ş Aydoğan, K. Çınar, H. Asıl, C. Coşkun, A. Türüt, J. Alloys Compd. **476**, 913 (2009)
59. S.R. Forrest, Chem. Rev. **97**, 1793 (1997)
60. G.H. Shin, J. Park, K.J. Lee, G.-B. Lee, H.B. Jeon, Y.-K. Choi, K. Yu, S.-Y. Choi, ACS Appl. Mater. Interfaces. **11**, 7626 (2019)
61. C. Bao, Z. Chen, Y. Fang, H. Wei, Y. Deng, X. Xiao, L. Li, J. Huang, Adv. Mater. **29**, 1703209 (2017)
62. Z.-M. Liao, C. Hou, L.-P. Liu, D.-P. Yu, Nanoscale Res. Lett. **5**, 926 (2010)
63. X. Zhang, J. Jie, W. Zhang, C. Zhang, L. Luo, Z. He, X. Zhang, W. Zhang, C. Lee, S. Lee, Adv. Mater. **20**, 2427 (2008)
64. C. Ling, T. Guo, W. Lu, Y. Xiong, L. Zhu, Q. Xue, Nanoscale. **9**, 8848 (2017)
65. S. Hubmann, S. Gebert, G.V. Budkin, V.V. Bel'kov, E.L. Ivchenko, A.P. Dmitriev, S. Baumann, M. Otteneder, J. Ziegler, D. Disterheft, D.A. Kozlov, N.N. Mikhailov, S.A. Dvoretsky, Z.D. Kvon, D. Weiss, S.D. Ganichev, Phys. Rev. B **99**, 085312 (2019)
66. A.K.K. Kyaw, D.H. Wang, V. Gupta, W.L. Leong, L. Ke, G.C. Bazan, A.J. Heeger, ACS Nano. **7**, 4569 (2013)
67. F. Yıldırım, H.F. Rouhi, H.M. Chenari, M. Biber, Ş Aydoğan, Sensors and Actuators A: Physical **390**, 116616 (2025)
68. E. Dalodière, M. Virot, V. Morosini, T. Chave, T. Dumas, C. Hennig, T. Wiss, O. Dieste Blanco, D.K. Shuh, T. Tyliszcak, L. Venault, P. Moisy, S.I. Nikitenko, Sci. Rep. **7**, 43514 (2017)
69. J. Wu, M. Wei, J. Mu, H. Ma, C. Zhong, Y. Ye, C. Sun, B. Tang, L. Wang, J. Li, X. Xu, B. Liu, L. Li, H. Lin, ACS Nano **15**, 15982 (2021)
70. H.F. Rouhi, F. Yıldırım, S. Nuhzat, H.M. Chenari, Ş Aydoğan, J. Alloys Compd. **1039**, 182952 (2025)
71. A. Khan, R.R. Kumar, J. Cong, M. Imran, D. Yang, X. Yu, Adv. Mater. Interfaces **9**, 2100977 (2022)
72. F. Yıldırım, K. Ganjehyan, M. Erdoğan, Ş. Aydoğan, ACS Appl. Electron. Mater. **7**, 10267 (2025)
73. T. Han, M. Shou, L. Liu, Z. Xie, L. Ying, C. Jiang, H. Wang, M. Yao, H. Deng, G. Jin, J. Chen, Y. Ma, J. Mater. Chem. C **7**, 4725 (2019)
74. A. Kocyigit, A.A. Hussaini, D.E. Yıldız, B. Gündüz, M. Yıldırım, Sens. Actuators A Phys. **394**, 116981 (2025)
75. J. Cong, A. Khan, P. Hang, L. Cheng, D. Yang, X. Yu, Nanotechnology **33**, 505201 (2022)
76. F. Yıldırım, S. Karakaya, H. Yuca, Ü. İncekara, Ş Aydoğan, J. Alloys Compd. **979**, 173584 (2024)
77. M. Ulusoy, S. Koçyiğit, A. Tataroğlu, S. Altındal Yerişkin, ACS Omega. **9**, 32243 (2024)
78. M. Bednorz, G.J. Matt, E.D. Głowacki, T. Fromherz, C.J. Brabec, M.C. Scharber, H. Sitter, N.S. Sariciftci, Org. Electron. **14**, 1344 (2013)
79. K. Ganjehyan, F. Yıldırım, M. Erdoğan, A. Daştan, Ş Aydoğan, Sens. Actuators A Phys. **367**, 115048 (2024)
80. U. Punia, P. Prajapat, R.K. Sharma, G. Jayant, Gupta, S.K. Srivastava, Next Mater. **8**, 100736 (2025)
81. A. Karaca, D.E. Yıldız, A.A. Hussaini, M. Yıldırım, B. Gündüz, Phys. B Condens. Matter **725**, 418225 (2026)
82. B. Barış, S. Karadeniz, S. Mirza, A.A. Hussaini, M. Yıldırım, D.E. Yıldız, J. Mater. Sci. Mater. Electron. **36**, 1390 (2025)
83. H.O. Dogan, F. Yıldırım, Z. Orhan, A. Ben Ahmed, M. Benhaliliba, Ş Aydoğan, Org. Electron. **124**, 106946 (2024)
84. T. Chandrakalavathi, M. Reddeppa, T. Revathi, P.K. Basivi, S.K. Viswanath, G. Murali, M.-D. Kim, R. Jeyalakshmi, Diam. Relat. Mater. **93**, 208 (2019)
85. A.A. Hussaini, Y. Torlak, S. Büyükçelebi, M. Kus, M. Yıldırım, Opt. Mater. **165**, 117144 (2025)
86. J. Cong, A. Khan, P. Hang, D. Yang, X. Yu, ACS Appl. Electron. Mater. **4**, 1715 (2022)